ORIGINAL RESEARCH

T$_1$–T$_2$ molecular magnetic resonance imaging of renal carcinoma cells based on nano-contrast agents

Jingjing Li[1,2,*]
Jia You[2,3,*]
Chen Wu[2]
Yue Dai[1]
Meilin Shi[2]
Lina Dong[2]
Kai Xu[1,2]

[1]Department of Radiology, Affiliated Hospital of Xuzhou Medical University, Xuzhou 221006, People's Republic of China; [2]School of Medical Imaging, Xuzhou Medical University, Xuzhou 221004, People's Republic of China; [3]Department of Radiology, Nanjing First Hospital, Nanjing Medical University, Nanjing 210006, People's Republic of China

*These authors contributed equally to this work

Correspondence: Kai Xu
Department of Radiology, Affiliated Hospital of Xuzhou Medical University, Xuzhou 221006, People's Republic of China
Tel +86 516 8580 2392
Fax +86 516 8326 2158
Email xkpaper@163.com

Background: The development of T$_1$–T$_2$ dual contrast agent (CA) favors the visualization of the lesion in a more accurate and reliable manner by magnetic resonance imaging (MRI). The relaxivity and the interference between T$_1$ and T$_2$ CA are the main concerns for their design.
Methods: In this work, we constructed an Fe$_3$O$_4$@mSiO$_2$/PDDA/BSA-Gd$_2$O$_3$ nanocomplex where BSA-Gd$_2$O$_3$ NPs and Fe$_3$O$_4$ NPs were chosen as T$_1$ and T$_2$ MRI CAs and a 20 nm mesoporous silica (mSiO$_2$) nanoshell was introduced to reduce the interference between them. We performed transmission electron microscopy, X-ray powder diffraction, UV-vis absorption spectra, and Fourier transform infrared absorption (FTIR) spectra to characterize the prepared nanocomplex and MRI scanning to evaluate their MRI behaviors. Furthermore, 3-(4,5-Dimethylthiazol-2-yl)-2,5-diphenyltetrazolium bromide (MTT) assay and hematologic and biochemical analyses were introduced to evaluate their in vitro and in vivo toxicity. Finally, the specific MRI of 786-0 cells with Fe$_3$O$_4$@mSiO$_2$/PDDA/BSA-Gd$_2$O$_3$-AS1411 nanoprobe in vitro was realized. In vivo biodistribution of Fe$_3$O$_4$@mSiO$_2$/PDDA/BSA-Gd$_2$O$_3$ nanocomplex in the mouse was determined by the quantification of the Gd element by inductively coupled plasma-mass spectrometry.
Results: The prepared Fe$_3$O$_4$@mSiO$_2$/PDDA/BSA-Gd$_2$O$_3$ nanocomplex possessed high longitudinal (r_1=11.47 mM s^{-1} Gd) and transverse (r_2=195.1 mM s^{-1} Fe) relaxivities, enabling its use as a T$_1$–T$_2$ dual contrast agent for MRI. MTT testing and hematologic and biochemical analysis indicated the good biocompatibility of Fe$_3$O$_4$@mSiO$_2$/PDDA/BSA-Gd$_2$O$_3$ nanocomplex in vitro and in vivo. After further conjugation with AS1411 aptamer, they could target tumor cells successfully by T$_1$ and T$_2$ MRI in vitro. The possible metabolic pathway of the tail vein-injected Fe$_3$O$_4$@mSiO$_2$/PDDA/BSA-Gd$_2$O$_3$ nanocomplex in mouse was mainly via kidney.
Conclusion: A T$_1$–T$_2$ dual-mode contrast agent, Fe$_3$O$_4$@mSiO$_2$/PDDA/BSA-Gd$_2$O$_3$ nanocomplex, was developed and its good performance for tumor cell targeting in vitro and kidney contrast-enhanced MRI in mice indicated its promising potential as an effective T$_1$–T$_2$ dual-mode contrast agent for in vivo MRI with self-confirmation.
Keywords: molecular magnetic resonance imaging, nano-contrast agent, aptamer, T$_1$–T$_2$, MRI

Introduction

Among the various biomedical imaging modalities, magnetic resonance imaging (MRI) – which provides high-resolution anatomical images in a noninvasive manner – is one of the most powerful tools.[1,2] In 40%–50% cases of clinical application, magnetic resonance (MR) contrast agents (CAs) are introduced to enhance the contrast, presenting improved sensitivity and quality of the images for more accurate diagnosis.[3] MRI CAs, generally in the form of T$_1$-positive and T$_2$-negative CAs, greatly improve the sensitivity of MRI by affecting the rate of water proton relaxation. For T$_1$-weighted CAs, paramagnetic

complexes containing gadolinium (Gd^{3+}) and manganese (Mn^{2+}) ions are commonly used to effectively accelerate the T_1 relaxation process to produce a brighter image.[4–9] In contrast, T_2-weighted CAs, such as the superparamagnetic iron oxide nanoparticles (SPIOs), exhibit strong magnetization when an external magnetic field is applied. This causes microscopic field inhomogeneity and activates the dephasing of protons to produce decreased signal intensity in T_2- and T_2^*-weighted MR images.[10,11] However, each modal CA has its own unique advantages and limitations. For example, the commonly used T_1 CAs are relatively small molecules, which are fast excreted by the kidneys, thereby resulting in difficulty with high-resolution image acquisition. Moreover, the functionalization of paramagnetic complexes with targeting molecules is hampered by the arduous and complex modification process.[12–14] On the other hand, SPIOs as T_2 MR CAs are very useful for biomedical applications because they are not subject to strong magnetic interactions in dispersion and are readily stabilized under physiological conditions.[15] However, the biggest issue with using T_2 CAs is that it is difficult to distinguish the signal from an air bubble or image artifact. Due to the negative contrast effect and susceptibility artifacts, it is difficult to distinguish the region of signals induced by SPIOs from low-level background MR signals, such as signals arising from adjacent tissues, bone, or vasculature.[11] Furthermore, independent T_1 or T_2 MR imaging suffers from false-positive signals that are ubiquitously observed in tissues. Last but not the least, T_1–T_2 dual imaging displays obvious advantages over single imaging with regard to water and fat molecules in tissue. For example, some tissue components such as the bone and fiber components present low signals on T_1WI similar to water. Moreover, some tissue components such as bleeding and mucus present high signals on the T_1WI similar to fat. It is difficult to distinguish water and fat with single imaging. However, with T_1–T_2 dual imaging, these issues can be addressed. Water presents a low signal on T_1WI

and a high signal on T_2WI. Fat presents a high signal on both T_1WI and T_2WI. Thus, it is easy to recognize water and fat with dual imaging. Therefore, the development of T_1–T_2 dual CAs is emerging attractively because they have the ability to validate reconstruction and visualization of the data in a more accurate and reliable manner, and to acquire complementary and self-confirmed information to permit meaningful interpretation.[16] Several kinds of dual CAs have been reported to improve the diagnostic accuracy of diseases.[17–24] Choi et al developed a nanoparticle (NP)-based dual CA – $MnFe_2O_4@SiO_2@Gd_2O(CO_3)_2$ – which not only possessed superior MR contrast effects, but also had the unique capability of displaying "AND" logic signals in both T_1 and T_2 modes.[22] Bae et al synthesized Gd-labeled Fe_3O_4 NPs and demonstrated their capability as dual CAs for T_1- and T_2-weighted MRI.[21]

For the design of T_1–T_2 dual CAs, two main aspects should be concerned. Firstly, to obtain high sensitivity, the T_1 and T_2 CAs themselves should possess good MRI relaxivities. High relaxivity is the primary requisite for the development of molecular imaging MR probes and targeting probes.[25–27] Several strategies for increasing the sensitivity (relaxivity) of MRI CAs have been well reviewed.[28–30] Secondly, the undesirable T_1 signal quenching of the paramagnetic T_1 CA by the magnetic field generated by a superparamagnetic T_2 CA when they are in proximity should be avoided. To address these issues, in this study, we aimed to synthesize the $Fe_3O_4@mSiO_2/PDDA/BSA-Gd_2O_3$ nanocomplex (Scheme 1) and explore its potential as a T_1–T_2 dual CA to obtain better MRI contrast enhancement and specific tumor cell targeting. BSA-Gd_2O_3 NPs and Fe_3O_4 NPs were chosen as T_1 and T_2 MRI CAs. High-Gd density paramagnetic ultrasmall gadolinium oxide nanoparticles (Gd_2O_3 NPs) have emerged to present larger T_1 relaxivity, good biocompatibility, and easy conjugation with other biomolecules or imaging agents for molecular MRI (mMRI) and multimodal molecular imaging.[18,31,32] The mesoporous silica nanoshell was introduced to coat Fe_3O_4 NPs and load BSA-Gd_2O_3 NPs as well as to act as a spacer to minimize
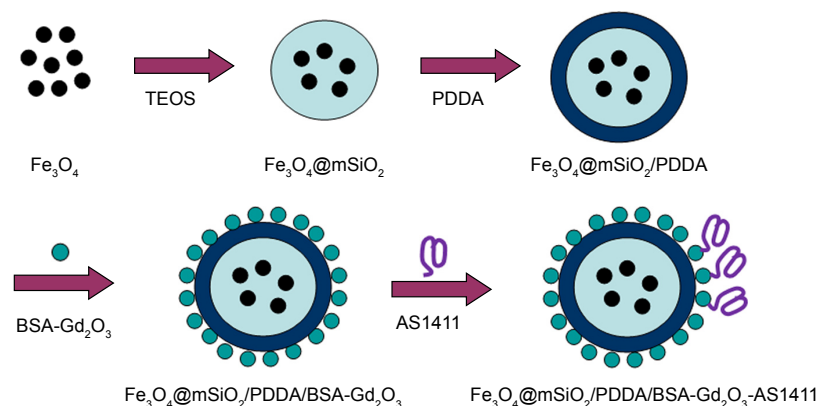
Scheme 1 Schematic illustration of the fabrication process of the $Fe_3O_4@mSiO_2/PDDA/BSA-Gd_2O_3$-AS1411 nanoprobes.

the magnetic spin interactions between T_1 and T_2 CAs. It has been proved that the magnetic field generated by a superparamagnetic T_2 CA could perturb the electronic spins of paramagnetic T_1 CA when they are in close proximity (<12 nm).[22] Furthermore, to realize the specific tumor cell imaging, an AS1411 aptamer, which can selectively bind with nucleolin overexpressed on a variety of cancer cells, was employed as the targeting molecule for the fabrication of the mMRI nanoprobe – Fe_3O_4@$mSiO_2$/PDDA/BSA-Gd_2O_3-AS1411.[33–35] Its ability for the specific targeting of renal cell carcinoma (RCC) was confirmed by the T_1–T_2-weighted MRI.

Materials and methods
Materials and reagents
Bovine serum albumin (BSA) was obtained from Solarbio (Beijing, People's Republic of China). $Gd(NO_3)_3 \cdot 6H_2O$, hexadecyl trimethyl ammonium bromide (CTAB), and dimethyl sulfoxide (DMSO) were purchased from Sinopharm Chemical Reagent Co. Ltd., Beijing, People's Republic of China Tetraethylorthosilicate (TEOS), poly(dimethyl diallyl ammonium chloride) (PDDA), 1-ethyl-3-(3-dimethylaminopropyl) carbodiimide hydrochloride (EDC·HCl), and N-hydroxysuccinimide (NHS) were purchased from Sigma-Aldrich (Saint Louis, MO, USA). DNA oligos were synthesized and purified by Shanghai Sangon Biotechnology Co. Ltd. (Shanghai, People's Republic of China); 3-(4,5-Dimethylthiazol-2-yl)-2,5-diphenyltetrazolium bromide (MTT) was obtained from Sunshine Biotech. Co. Ltd. (Nanjing, People's Republic of China). Cell culture media including HDMEM, RPMI 1640, and fetal calf serum were obtained from Kangmei Biotechnology Co. Ltd (Xuzhou, People's Republic of China). All other reagents were of analytical grade and used without purification. All aqueous solutions were prepared using ultrapure water from a Milli-Q system (Millipore, Boston, MA, USA). The DNA sequence is listed as follows.

COOH-AS1411:

5′-COOH-GGTGGTGGTGGTTGTGGTGGTG GTGG-3′.

Apparatus and characterization
The size and morphology of NPs were observed by transmission electron microscopy (TEM; TECNAI G2, FEI Company, Hillsboro, OR, USA). Fourier transform infrared absorption (FTIR) spectra were obtained through FTIR spectroscopy (Bruker, Billerica, MA, USA). Zeta potentials were determined by Nano ZS90 (Malvern Panalytical Ltd, Malvern, England). X-ray powder diffraction (XRD) patterns were obtained by using a X-ray powder diffractometer (D8 ADVANCE, Bruker). The determinations of Gd and iron ion concentrations were undertaken with inductively coupled plasma-mass spectrometry (ICP-MS) (Optima 5300DV, PerkinElmer, San Diego, CA, USA). The absorbances for MTT assay were determined by a microplate reader (Multiskan MK3, Thermo Fisher Scientific, Waltham, MA, USA) at 490 nm. MRI scanning was conducted on a Signa HDxt 3.0T, General Electric Company, Boston, Massachusetts, USA. Hematologic and biochemical analysis was carried out with a hematology analyzer (Mindray BC-5390, Mindray Bio-Medical Electronics Co., Ltd., Shenzhen, People's Republic of China) and cobas connection modules (Roche Diagnostics, Basel, Switzerland), respectively.

Cells and cell culture conditions
The 786-0 renal carcinoma cells and NIH-3T3 mouse fibroblast cells were purchased from the Cell Bank of the Chinese Academy of Sciences (Shanghai, People's Republic of China). The 786-0 renal carcinoma cells were cultured in a 10% FBS-containing RPMI 1640 medium (Sijiqing, People's Republic of China) supplemented with penicillin (100 mg/mL) and streptomycin (100 mg/mL). NIH-3T3 cells were propagated in 10% FBS-containing Dulbecco's Modified Eagle's Medium (Gibco, Grand Island, NY, USA) supplemented with penicillin (100 mg/mL) and streptomycin (100 mg/mL). All cells were grown in a humidified incubator (Thermo Fisher Scientific) at 37°C under 5% CO_2 atmosphere.

Preparation of Fe_3O_4 NPs
The Fe_3O_4 NPs were synthesized using a previously reported method.[36] In brief, approximately 10 mL water containing 1.0 mol/L Fe^{3+} and 0.5 mol/L Fe^{2+} ions (molar ratio 2:1) was stirred at 400 rpm on a stir plate for 20 min. Then, 30 mL ammonium hydroxide was slowly added to the solution and the speed was increased to 900 rpm in order to uniformly precipitate magnetic NPs. Fe_3O_4 NPs were obtained 30 min later. They were washed with distilled water until the pH value decreased to 7.0. Finally, the obtained Fe_3O_4 NPs were dispersed in distilled water at a concentration of 0.24 mg/mL until further use.

Synthesis of Fe_3O_4@$mSiO_2$ core-shell NPs
In a typical procedure,[37] CTAB (50 mg) was dissolved in 20.8 mL distilled water. In total, 4.2 mL Fe_3O_4 and NaOH solution (2.00 M, 160 µL) were added to the above CTAB solution sequentially. Then, the mixture was heated to 70°C with stirring, and 250 µL TEOS and 500 µL ethylacetate were added to the reaction solution in sequence. The mixture was stirred for 3 h at 70°C. The resultant precipitate was washed 3 times with ethanol to remove the unreacted species and then dispersed in 20 mL ethanol. To extract CTAB, 20 µL HCl was added to the dispersion mixture (pH>1.0) and stirred for 3 h

at 60°C. To obtain hollow mesoporous silica, more HCl was used for extraction (pH <1.0). After washing three times with ethanol, the Fe_3O_4@$mSiO_2$ NPs were dried at 50°C.

Preparation of BSA-Gd_2O_3 NPs

BSA-Gd_2O_3 NPs were synthesized according to the methods specified in the literature with some modifications.[38] In total, 0.25 g BSA was dissolved in 9 mL distilled water. Then, 1 mL 50 mM $Gd(NO_3)_3$ was added to the above solution slowly under vigorous stirring. After the introduction of 1 mL 2 M NaOH 5 min later, the mixture was allowed to react under vigorous stirring at 37°C for 12 h. Finally, the BSA-Gd_2O_3 thus prepared was dialyzed against distilled water (1:1,000, v/v) to remove excess precursors.

Fabrication of Fe_3O_4@$mSiO_2$/PDDA/ BSA-Gd_2O_3-AS1411 mMRI nanoprobe

The Fe_3O_4@$mSiO_2$/PDDA/BSA-Gd_2O_3 was prepared through electrostatic interaction.[39] Initially, Fe_3O_4@$mSiO_2$ (3 mg) and PDDA solution (2 mL, 2 mg/mL, 0.2 M NaCl) were mixed under sonication for 40 min, and the excess polyelectrolyte was removed by washing with water. Then, the positively charged magnetic particles were dispersed in distilled water (500 μL), and BSA-Gd_2O_3 (50 μL, 1.06 μM Gd) was added and sonicated for 40 min. After washing with water, the Fe_3O_4@$mSiO_2$/PDDA/BSA-Gd_2O_3 were dispersed in 2 mL water for MRI scanning. Meanwhile, to obtain the best MRI behavior, different concentrations of BSA-Gd_2O_3 NPs (0.212, 0.636, 1.06, 1.484, and 1.908 μM Gd) and Fe_3O_4 (1, 3, and 5 mg) were tested. At the optimized condition, the AS1411 aptamer was functionalized onto the surface of Fe_3O_4@$mSiO_2$/PDDA/ BSA-Gd_2O_3 NPs by covalent coupling between the amino group of BSA-Gd_2O_3 and the carboxyl group modified at the 5′ end of AS1411 aptamer with the help of EDC and NHS.[40] Briefly, 100 μM COOH-AS1411 (50 μL) was mixed with EDC (100 μL, 10 mg mL^{-1}) in 300 μL PBS (10 mM, pH 7.4) and incubated at 37°C for 15 min to form an active carboxyl group. Then, NHS (100 μL, 10 mg mL^{-1}) and Fe_3O_4@$mSiO_2$/PDDA/ BSA-Gd_2O_3 (500 μL, 5.0 mg mL^{-1}) were added to the mixture and reacted at 37°C for 2 h. The unreacted biomolecules were removed by two centrifugation/washing cycles. Finally, the Fe_3O_4@$mSiO_2$/PDDA/BSA-Gd_2O_3-AS1411 nanoprobes were dispersed in 1 mL PBS (10 mM) at pH 7.4 for further use.

Relaxivity calculation of Fe_3O_4 NPs, BSA-Gd_2O_3 NPs, Gd-DTPA, and Fe_3O_4@ $mSiO_2$/PDDA/BSA-Gd_2O_3 nanocomplex

The MRI behavior test of BSA-Gd_2O_3 and Fe_3O_4 was conducted with a 3.0 T human MR scanner (General Electric Company).

Various concentrations of BSA-Gd_2O_3 and Fe_3O_4 solution were prepared before MRI scanning, which varied from 0.212 to 1.908 μM with a volume of 600 μL for BSA-Gd_2O_3 NPs, and 1–5 mg for Fe_3O_4 NPs. The following parameters were adopted in data acquisition. 1) T_1-weighted images: echo time (TE)=16.5 ms, repetition time (TR)=420 ms, field of view (FOV)=14×14 cm, matrix=384×256, slice thickness=2.0 mm, spacing=0.2 mm; and 2) T_2-weighted images: echo time (TE)=90.7 ms, repetition time (TR)=4,500 ms, field of view (FOV)=14×14 cm, matrix=384×256, slice thickness=2.0 mm, spacing=0.2 mm. Quantitative T_1 and T_2 relaxation maps were reconstructed from datasets using function software at a workstation (ADW 4.2). The signal intensities of the samples were measured, and the T_1 and T_2 values were calculated accordingly. MRI scanning of Gd-DTPA and the Fe_3O_4@$mSiO_2$/PDDA/BSA-Gd_2O_3 nanocomplex with different concentrations was carried out in the same way.

The T_1 relaxivity values of the BSA-Gd_2O_3, Gd-DTPA, and Fe_3O_4@$mSiO_2$/PDDA/BSA-Gd_2O_3 nanocomplex were determined by measuring longitudinal proton relaxation time (T_1) as a function of Gd concentration. The T_2 relaxivity values of the Fe_3O_4 and Fe_3O_4@$mSiO_2$/PDDA/BSA-Gd_2O_3 nanocomplex were determined by measuring the lateral proton relaxation time (T_2) as a function of Fe concentration.

MTT assay

The 786-0 cells and NIH-3T3 cells were cultured on 96-well plates at a density of 10^4 cells each well. After 24-h incubation, the medium was substituted with 100 μL fresh medium containing different concentrations of the Fe_3O_4@$mSiO_2$/ PDDA/BSA-Gd_2O_3 nanocomplex (0, 200, 400, 600, 800, 1,000, 1,200, and 1,400 μg mL^{-1}). After 24-h incubation, the medium was removed, and fresh medium (100 μL) containing MTT (20 μL, 5 mg mL^{-1}) was added into each well. Four hours later, the culture medium was carefully removed and washed, and 100 mL DMSO was added to each well to dissolve the formazan crystals for 10 min. The absorbance at 490 nm was measured by a microplate reader (Multiskon MK3, USA).

Stability test

The Fe_3O_4@$mSiO_2$/PDDA/BSA-Gd_2O_3 nanocomplex was dispersed in RPMI 1640 culture medium. At different time points (0, 2, 4, 6, 8, 12, 24, 48, and 72 h), 100 μL samples were collected and centrifuged at 25,000 rpm for 30 min to obtain the supernatant. The concentrations of Fe and Gd ions in the supernatant were determined by ICP-MS. For the pH stability test, the Fe_3O_4@$mSiO_2$/PDDA/BSA-Gd_2O_3 nanocomplex was dispersed in solutions of different pHs (pH 4, 5, 6, 7, 8, 9, and 10) and incubated for 24 h. The concentrations determined for Fe and Gd ions were the same as mentioned earlier.

Specific MR imaging of 786-0 cells with Fe_3O_4@$mSiO_2$/PDDA/BSA-Gd_2O_3-AS1411 mMRI nanoprobe in vitro

The 786-0 cells and NIH-3T3 cells were seeded into six-well plates at a density of 10^5 cells/well and cultured for 24 h in a humidified incubator at 37°C under 5% CO_2 atmosphere, respectively. Then, the culture media was removed and the cells were washed with PBS twice. In total, 500 µL of different concentrations of Fe_3O_4@$mSiO_2$/PDDA/BSA-Gd_2O_3-AS1411 nanoprobe (0.5, 1, and 2.5 mg mL^{-1}) and Fe_3O_4@$mSiO_2$/PDDA/BSA-Gd_2O_3 nanocomplex (0.5, 1, and 2.5 mg mL^{-1}) were added into the well and incubated for 1 h at 37°C. After discarding the nanoprobe, the cells were washed and lysed by trypsin. The harvested cells were fixed with 600 µL 1% agarose for MRI scanning. The untreated cells that were incubated with PBS were taken as the control.

Biodistribution of the Fe_3O_4@$mSiO_2$/PDDA/BSA-Gd_2O_3 nanocomplex in the mouse

The residual nanocomplex in heart, liver, kidneys, and lungs after 1 h and 24 h post-injection of the Fe_3O_4@$mSiO_2$/PDDA/BSA-Gd_2O_3 nanocomplex was determined by the quantification of the Gd element by ICP-MS. Briefly, six Kunming mice were divided into two groups: 1-h post-injection and 24-h post-injection. Each mouse was injected with the same concentration of the Fe_3O_4@$mSiO_2$/PDDA/BSA-Gd_2O_3 nanocomplex (0.16 mmol Gd per kg body weight). The mice were sacrificed and the major organs, including heart, liver, kidneys, and lungs, were collected at 1 h and 24 h post-injection. To these organs, 2 mL aqua regia (HCl:HNO_3=3:1) was added and the organs in aqua regia were heated to 200°C for 1 h. After being cooled to room temperature, 2 mL H_2O was added and a 0.22-µm filter was introduced to remove undigested tissues.[41] The Gd concentrations were then analyzed by ICP-MS.

In vivo toxicity evaluation of Fe_3O_4@$mSiO_2$/PDDA/BSA-Gd_2O_3 nanocomplex

Hematologic and biochemical analyses were introduced to evaluate the in vivo toxicity of the Fe_3O_4@$mSiO_2$/PDDA/BSA-Gd_2O_3 nanocomplex. In total, six Kunming mice were divided into two groups: the normal saline group and the Fe_3O_4@$mSiO_2$/PDDA/BSA-Gd_2O_3 nanocomplex group. The mice were injected with normal saline and the Fe_3O_4@$mSiO_2$/PDDA/BSA-Gd_2O_3 nanocomplex (0.16 mmol Gd per kg body weight) via tail vein, respectively. After 1 week, blood was harvested by cardiac puncture. Hematologic analysis including platelets (PLT), hematocrit (HCT), hemoglobin (HGB), red blood cells (RBC), white blood cells (WBC), mean

corpuscular volume (MCV), mean corpuscular hemoglobin (MCH), and mean corpuscular hemoglobin concentration (MCHC) was undertaken on a hematology analyzer. The biochemical effects of the Fe_3O_4@$mSiO_2$/PDDA/BSA-Gd_2O_3 nanocomplex for alanine transaminase (ALT), aspartate transaminase (AST), blood urea nitrogen (BUN), creatinine (CREA), total protein (TP), albumin (ALB), and total bilirubin (TBIL) were evaluated by cobas connection modules.

In vivo MRI

Animal experiments were conducted in accordance with the National Institutes of Health guidelines on the use of animals in research, and were approved by the Animal Care Committee of Xuzhou Medical University. Healthy BALB/c mice weighing 20–30 g were chosen for in vivo MRI study. The mice were anesthetized by intraperitoneal injection of 2% mebumalnatrium (4 µL/g bodyweight), followed by tail-vein administration of the Fe_3O_4@$mSiO_2$/PDDA/BSA-Gd_2O_3 nanocomplex (0.16 mmol Gd per kg body weight). Then, at scheduled intervals, T_1WI images and T_2WI images were acquired by a 3.0 T MR imaging system (GE Discovery 750W, USA) with the animal T/R coil (Magtron Inc., Jiangyin, People's Republic of China). The sequences for T_1-weighted images were set as follows: TE=12 ms; TR=400 ms; FOV=80×80 mm; slice thickness=2 mm; spacing=0.2 mm; and matrix=256×256. The sequences for T_2-weighted images were set as follows: TE=58 ms; TR=300 ms; FOV=80×48 mm; slice thickness=2 mm; spacing=0.2 mm; and matrix=256×256. To compare the signal intensity at different time points, the same protocols, prone position, and the same scanning landmark of MRI were required. The relative intensity changes of the same region of interest on the same slice in the same window width and window level were recorded by software in the workstation GE AW4.6.

Results

Characterization of Fe_3O_4@$mSiO_2$/PDDA/BSA-Gd_2O_3-AS1411 mMRI nanoprobe

For the fabrication of the T_1–T_2 dual CA, 10.7-nm-sized-Fe_3O_4 NPs as T_2 CA were first encased with an $mSiO_2$ nanoshell (Figure S1). An approximately 20-nm nanoshell could reduce the quenching effect of Fe_3O_4 NPs on the T_1 signal to the extent that was possible. Then, BSA-Gd_2O_3 NPs were deposited onto the Fe_3O_4@$mSiO_2$ surface through layer-by-layer assembly with the help of polyelectrolytes and PDDA. Driven by the electrostatic force, a uniform monolayer of positively charged PDDA and negatively charged BSA-Gd_2O_3 NPs were alternatively adsorbed onto
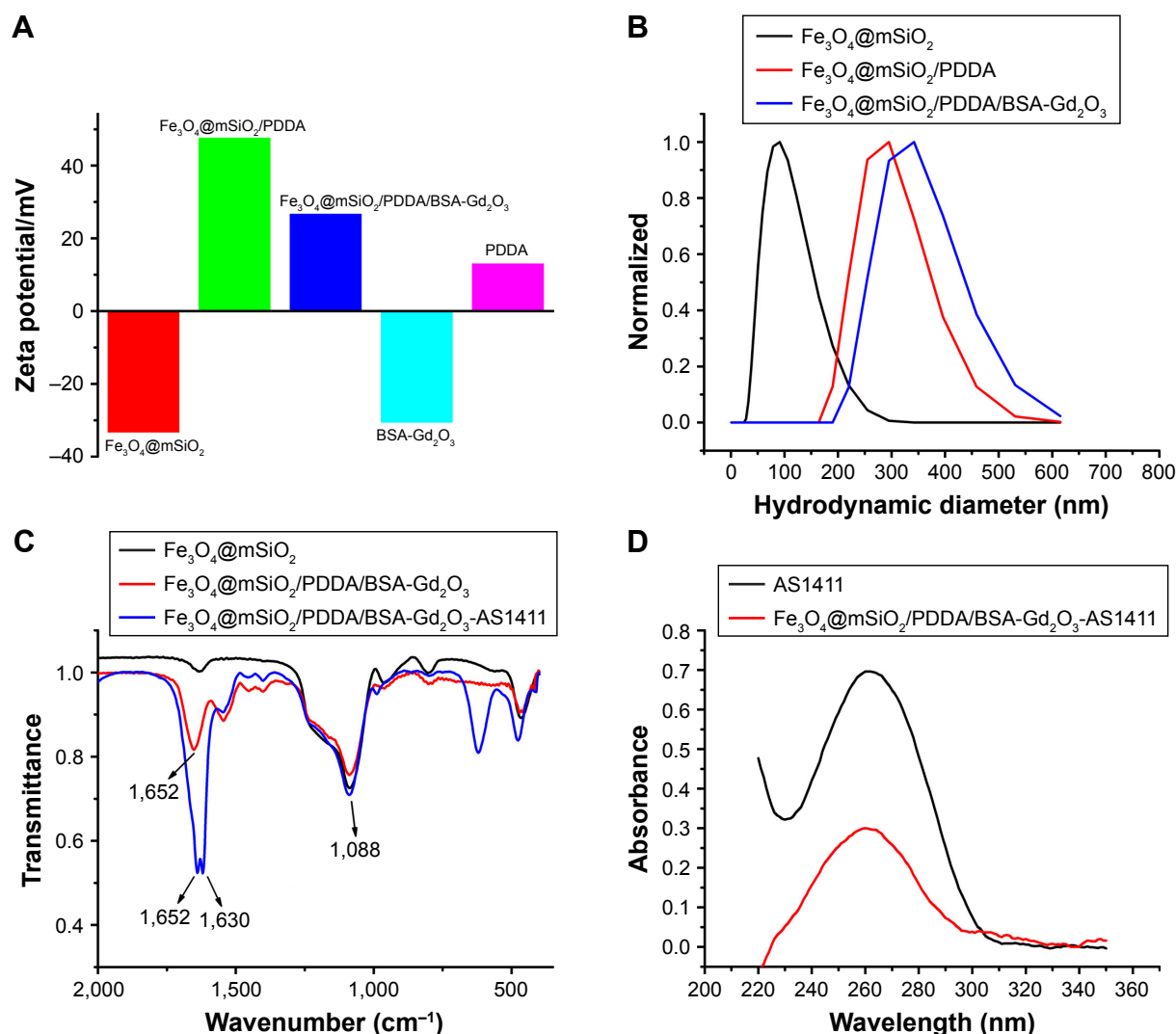
Figure 1 Characterization of the assembly process of $Fe_3O_4@mSiO_2/PDDA/BSA-Gd_2O_3$ with zeta potential (**A**), hydrodynamic diameter determination (**B**), and the fabrication of the $Fe_3O_4@mSiO_2/PDDA/BSA-Gd_2O_3-AS1411$ nanoprobe with fourier transform infrared absorption (FTIR) spectra (**C**) and UV-vis spectra (**D**).

the negatively charged $Fe_3O_4@mSiO_2$ NPs. This assembly process was monitored by the determination of the changes of zeta potentials. As shown in Figure 1A, the potential value of $Fe_3O_4@mSiO_2$ NPs was −33.5 mV and changed to 47.8 mV with PDDA assembly. The zeta potential of the $Fe_3O_4@mSiO_2/PDDA/BSA-Gd_2O_3$ nanocomplex was 26.9 mV, which might derive from the negatively charged BSA. The corresponding hydrodynamic diameters of $Fe_3O_4@mSiO_2$, $Fe_3O_4@mSiO_2/PDDA$ and $Fe_3O_4@mSiO_2/PDDA/BSA-Gd_2O_3$ were changed from 100.2 to 297.4 and 345.6 nm, accordingly (Figure 1B). From XRD patterns in Figure S2, the typical diffraction peaks of Fe_3O_4 were observed. The amorphous hump of SiO_2 at around 26° and the characteristic peaks of Fe_3O_4 could be observed in $Fe_3O_4@mSiO_2$ and $Fe_3O_4@mSiO_2/PDDA/BSA-Gd_2O_3$, indicating the successful fabrication of the nanocomplex.[42] Then, the further conjugation of the AS1411 aptamer with the

$Fe_3O_4@mSiO_2/PDDA/BSA-Gd_2O_3$ nanocomplex through a covalent coupling reaction was confirmed by the FTIR absorption spectrum and UV-vis absorption spectrum. The emerging absorption peak at 1,630 and 1,652 cm^{-1} was ascribed to acyl-amide vibration in the FTIR absorption spectrum (Figure 1C), and a characteristic UV-vis absorbance peak of the AS1411 aptamer could be observed in the $Fe_3O_4@mSiO_2/PDDA/BSA-Gd_2O_3-AS1411$ nanoprobe (Figure 1D), both indicating the successful preparation of the mMRI nanoprobe.

MRI behavior of $Fe_3O_4@mSiO_2/PDDA/BSA-Gd_2O_3$ nanocomplex

To explore its potential as an mMRI nanoprobe, the MRI behavior of our synthesized $Fe_3O_4@mSiO_2/PDDA/BSA-Gd_2O_3$ nanocomplex was first evaluated. With different concentrations of $BSA-Gd_2O_3$ NPs, the T_1 and T_2 relaxation
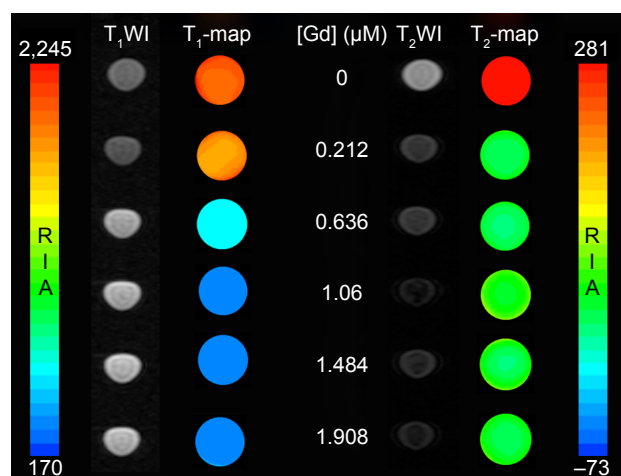
Figure 2 T_1-weighted magnetic resonance (MR) images and T_1-map images as well as T_2-weighted MR images and T_2-map images of the Fe_3O_4@mSiO$_2$/PDDA/BSA-Gd$_2$O$_3$ nanocomplex prepared with different concentrations of BSA-Gd$_2$O$_3$ NPs. 3.0 T human magnetic resonance scanner was used.

times of the Fe_3O_4@mSiO$_2$/PDDA/BSA-Gd$_2$O$_3$ nanocomplex varied. As shown in Figures 2 and 3, with the increase of the BSA-Gd$_2$O$_3$ NP concentration, the T_1 relaxation time of the Fe_3O_4@mSiO$_2$/PDDA/BSA-Gd$_2$O$_3$ nanocomplex was enhanced and reached a maximum of approximately 320 ms in the presence of 1.06 μM Gd. However, the further increased concentration of BSA-Gd$_2$O$_3$ NPs (1.484 and 1.908 μM Gd) influenced the T_1 relaxation time of the Fe_3O_4@mSiO$_2$/PDDA/BSA-Gd$_2$O$_3$ nanocomplex non-obviously. Unlike the T_1 relaxation time, the T_2 relaxation time of Fe_3O_4@mSiO$_2$/PDDA/BSA-Gd$_2$O$_3$ nanocomplex changed irregularly with the increase in the concentration of BSA-Gd$_2$O$_3$ NP. However,
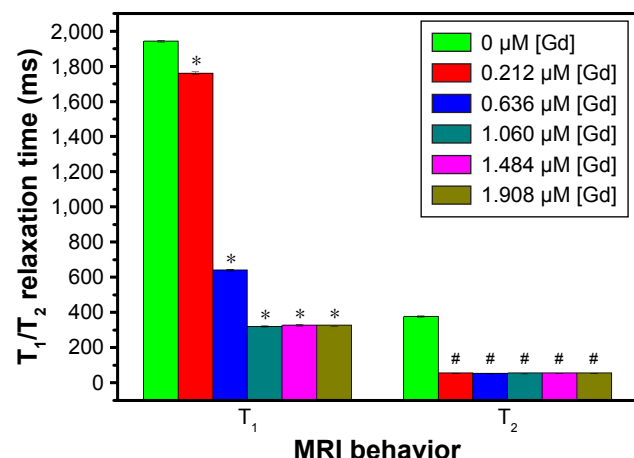

Figure 3 T_1 and T_2 relaxation time of the Fe_3O_4@mSiO$_2$/PDDA/BSA-Gd$_2$O$_3$ nanocomplex prepared with different concentrations of BSA-Gd$_2$O$_3$ NPs. BSA-Gd$_2$O$_3$ NPs (0 μM) were treated as the control group, and other groups were all compared with the control group with one-way ANOVA. *Refers to statistically significant differences compared with the control group with one-way ANOVA (p<0.05). #Refers to statistically significant differences compared with control group with one-way ANOVA (p<0.05). A 3.0 T human magnetic resonance scanner was used.

when the BSA-Gd$_2$O$_3$ NP concentration was 1.06 μM Gd, the T_2-map color image was darkest. The influence of Fe_3O_4 concentrations on the T_1 and T_2 relaxation times were not as strong as that of BSA-Gd$_2$O$_3$ NPs. As shown in Figure S3 and Table S1, with the increase of the Fe_3O_4 concentration, the T_1 relaxation time of the Fe_3O_4@mSiO$_2$/PDDA/BSA-Gd$_2$O$_3$ nanocomplex was weakened; however, its T_2 relaxation time changed little. For overall consideration, 50 μL 1.06 μM BSA-Gd$_2$O$_3$ and 1 mg Fe_3O_4 NPs were chosen for the fabrication of the Fe_3O_4@mSiO$_2$/PDDA/BSA-Gd$_2$O$_3$ nanocomplex in the following experiments.

To testify the influence of BSA-Gd$_2$O$_3$ NPs of our nanocomplex on T_2WI, we also synthesized the Fe_3O_4@mSiO$_2$ nanocomplex and the mSiO$_2$/PDDA/BSA-Gd$_2$O$_3$ nanocomplex. As shown in Figure S4 and Table S2, the T_2 signals of the Fe_3O_4@mSiO$_2$/PDDA/BSA-Gd$_2$O$_3$ nanocomplex and the Fe_3O_4@mSiO$_2$ nanocomplex were all less than the T_2 signal of the mSiO$_2$/PDDA/BSA-Gd$_2$O$_3$ nanocomplex; however, there was little change between the T_2 signal of the Fe_3O_4@mSiO$_2$/PDDA/BSA-Gd$_2$O$_3$ nanocomplex and the T_2 signal of the Fe_3O_4@mSiO$_2$ nanocomplex. Thus, in our prepared nanocomplex, the BSA-Gd$_2$O$_3$ NPs had no obvious effect on T_2WI, and Fe_3O_4 NPs influenced the T_2 signal obviously. From the above results, we can conclude that, for the synthesis of T_1–T_2 dual MRI CA Fe_3O_4@mSiO$_2$/PDDA/BSA-Gd$_2$O$_3$, T_1 and T_2 signals are ascribed to the BSA-Gd$_2$O$_3$ NPs and Fe_3O_4 core, respectively.

Then, the T_1 relaxivity values of Gd-DTPA, BSA-Gd$_2$O$_3$ NPs, and the Fe_3O_4@mSiO$_2$/PDDA/BSA-Gd$_2$O$_3$ nanocomplex were determined and compared by measuring longitudinal proton relaxation time (T_1) as a function of Gd concentration. As shown in Figure 4, the r_1 value of BSA-Gd$_2$O$_3$ was 12.2 s^{-1} mM^{-1}, which was three times that of the commercial MRI CAs, Gd–DTPA (r_1=4.3 s^{-1} mM^{-1}). The T_1 relaxivity of Fe_3O_4@mSiO$_2$/PDDA/BSA-Gd$_2$O$_3$ nanocomplex was 11.5 s^{-1} mM^{-1}. For the determination of the T_2 relaxivity values of Fe_3O_4 and the Fe_3O_4@mSiO$_2$/PDDA/BSA-Gd$_2$O$_3$ nanocomplex, lateral proton relaxation times (T_2) as a function of Fe concentration were measured. The T_2 relaxivity of the Fe_3O_4@mSiO$_2$/PDDA/BSA-Gd$_2$O$_3$ (195.1 s^{-1} mM^{-1} Fe) was lower than that of Fe_3O_4 (345.9 s^{-1} mM^{-1} Fe), but higher than the clinically used Feridex (108 s^{-1} mM^{-1} Fe)[1] and the relaxivity reported for Fe_3O_4@mSiO$_2$ NPs (171.6 s^{-1} mM^{-1} Fe; Figure 5).[43,44] Such excellent MR imaging behavior indicated the ability of the Fe_3O_4@mSiO$_2$/PDDA/BSA-Gd$_2$O$_3$ nanocomplex (the molar value of Fe/Gd equals 0.539; r_1/r_2 equals 0.0567) as a promising T_1–T_2 dual MRI CA for the fabrication of an mMRI nanoprobe to specifically image tumor cells.
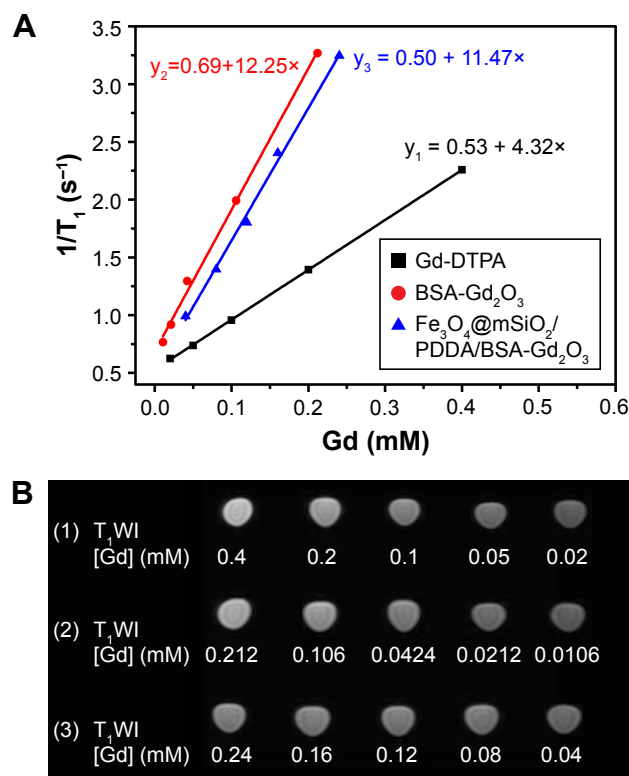
Figure 4 T_1 relaxivity curves (**A**) and T_1-weighted magnetic resonance (MR) images (**B**) of Gd-DTPA (1), BSA-Gd$_2$O$_3$ NPs (2), and Fe$_3$O$_4$@mSiO$_2$/PDDA/BSA-Gd$_2$O$_3$ nanocomplex (3) with various Gd concentrations. A 3.0 T human MR scanner was used.

In vitro cytotoxicity test

Before the use of the Fe$_3$O$_4$@mSiO$_2$/PDDA/BSA-Gd$_2$O$_3$ nanocomplex for specific tumor cell imaging, it is vital to assess its safety in vitro. The MTT assay was conducted to

evaluate the cell toxicity of the nanocomplex and identify potentially safe concentrations for the following targeting experiments. The Fe$_3$O$_4$@mSiO$_2$/PDDA/BSA-Gd$_2$O$_3$ nanocomplex with eight different concentrations, ranging from 0 to 1,400 µg/mL, was incubated with 786-0 and NIH-3T3 cells for 24 h, respectively. As shown in Figure 6, the Fe$_3$O$_4$@mSiO$_2$/PDDA/BSA-Gd$_2$O$_3$ nanocomplex displayed good biocompatibility, and no significant cytotoxicity was observed both on 786-0 renal carcinoma or NIH-3T3 cells.

Stability test

The leaching of metallic ions is a potential harmful effect of their biological application. To test the possibility of Gd and Fe ions leaching from the nanocomplex in biological media, we determined the concentrations of Gd and Fe ions in the supernatant with the passage of time from when the nanocomplex was dispersed in the cell culture medium and in different pH solutions incubated for 24 h. As shown in Figure 7, no obvious Gd and Fe ion leaching could be observed with time in the cell culture medium or different pH solutions, indicating the good stability of our fabricated nanocomplex.

In vitro specific T_1–T_2 dual MR imaging of tumor cells

Finally, the specific cellular targeting of the Fe$_3$O$_4$@mSiO$_2$/PDDA/BSA-Gd$_2$O$_3$-AS1411 mMRI nanoprobe was evaluated by T_1–T_2 MRI. AS1411 is a nucleolus of specific nucleic acid aptamers, which can specifically combine with nucleolin
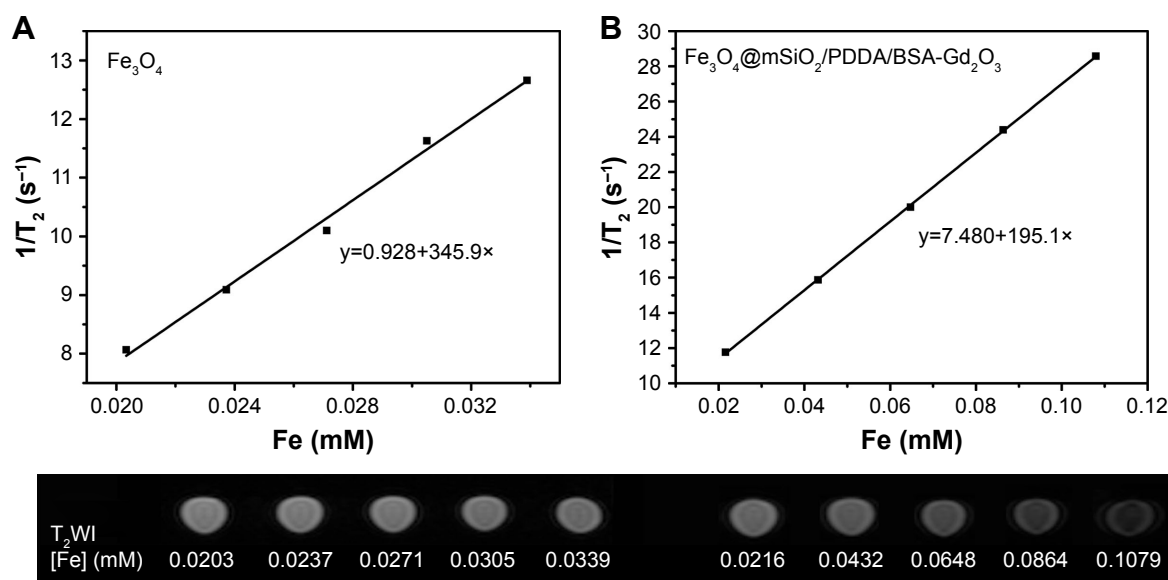

Figure 5 T_2 relaxivity curves and T_2-weighted magnetic resonance (MR) images of the Fe$_3$O$_4$ (**A**), and Fe$_3$O$_4$@mSiO$_2$/PDDA/BSA-Gd$_2$O$_3$ nanocomplex (**B**) with various Fe$_3$O$_4$ nanoparticle concentrations. A 3.0 T human MR scanner was used.
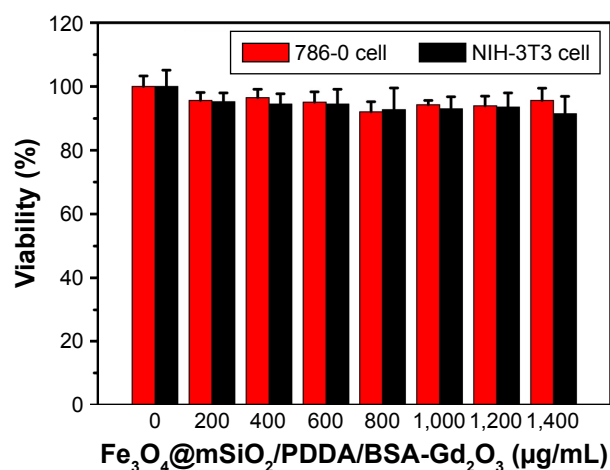
Figure 6 Cell viability of 786-0 renal carcinoma cells and NIH-3T3 mouse fibroblast cells after exposure to various concentrations of the Fe$_3$O$_4$@mSiO$_2$/PDDA/BSA-Gd$_2$O$_3$ nanocomplex, determined by 3-(4,5-Dimethylthiazol-2-yl)-2,5-diphenyltetrazolium bromide (MTT) assay.

on the surface of the tumor cell. As shown in Figure S5, the AS1411 modification did not produce a significant influence on the MRI behavior of the Fe$_3$O$_4$@mSiO$_2$/PDDA/BSA-Gd$_2$O$_3$ nanocomplex, indicating the potential use of the Fe$_3$O$_4$@mSiO$_2$/PDDA/BSA-Gd$_2$O$_3$-AS1411 as an mMRI nanoprobe.

To validate the specific targeting ability of the Fe$_3$O$_4$@mSiO$_2$/PDDA/BSA-Gd$_2$O$_3$-AS1411 mMRI nanoprobe, the 786-0 cells were incubated with the Fe$_3$O$_4$@mSiO$_2$/PDDA/BSA-Gd$_2$O$_3$ nanocomplex and Fe$_3$O$_4$@mSiO$_2$/PDDA/BSA-Gd$_2$O$_3$-AS1411 mMRI nanoprobes, respectively. For the achievement of the best signal-to-noise value, 0.5, 1, and 2.5 mg mL^{-1} nanoprobes were introduced and compared. As shown in Figures 8 and 9, the higher the concentration of

the Fe$_3$O$_4$@mSiO$_2$/PDDA/BSA-Gd$_2$O$_3$-AS1411 nanoprobe, the brighter the T_1 signal intensity and the darker the T_2 signal intensity from 786-0 cells. Furthermore, the presence of the AS1411 aptamer could facilitate more of the Fe$_3$O$_4$@mSiO$_2$/PDDA/BSA-Gd$_2$O$_3$-AS1411 nanoprobe to bind with 786-0 cells and present a brighter T_1 signal and a darker T_2 signal at all three concentrations. However, when the concentration of the nanoprobe reached 2.5 mg mL^{-1}, the nonspecific adsorption obviously increased. Thus, 1 mg mL^{-1} of the Fe$_3$O$_4$@mSiO$_2$/PDDA/BSA-Gd$_2$O$_3$-AS1411 nanoprobe was chosen for the specific MRI finally. To further confirm such AS1411 aptamer-based specific targeting, NIH-3T3 cells were introduced as the control and treated with 1 mg of the mL^{-1} Fe$_3$O$_4$@mSiO$_2$/PDDA/BSA-Gd$_2$O$_3$-AS1411 nanoprobe, Fe$_3$O$_4$@mSiO$_2$/PDDA/BSA-Gd$_2$O$_3$ nanocomplex, respectively. No significant difference existed between these two groups in both T_1 and T_2 signal, indicating the specific MRI ability of our synthesized nanoprobe to ccRCC in vitro (Figure S6, Tables S3 and S4).

Biodistribution of the Fe$_3$O$_4$@mSiO$_2$/PDDA/BSA-Gd$_2$O$_3$ nanocomplex in the mouse

To show the biodistribution and residual persistence of the Fe$_3$O$_4$@mSiO$_2$/PDDA/BSA-Gd$_2$O$_3$ nanocomplex in different organs, ICP-MS was employed to determine the Gd concentration in the heart, liver, kidneys, and lungs after 1 h and 24 h following injection of the Fe$_3$O$_4$@mSiO$_2$/PDDA/BSA-Gd$_2$O$_3$ nanocomplex. As shown in Figure 10, the Gd concentration in the above organs all decreased, except in the kidney.
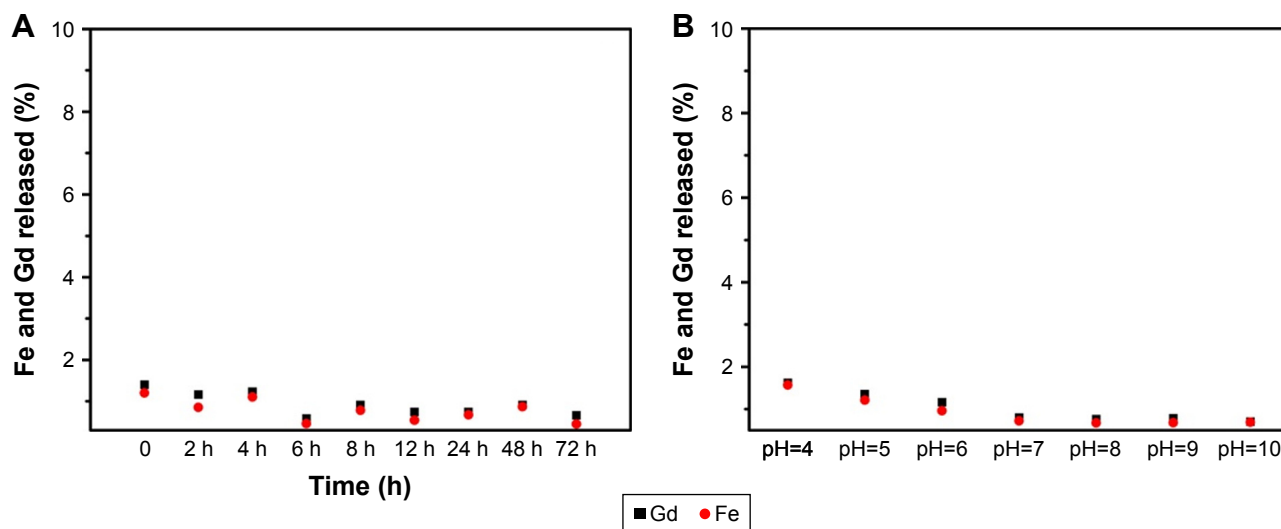

Figure 7 Iron and gadolinium ions released from the Fe$_3$O$_4$@mSiO$_2$/PDDA/BSA-Gd$_2$O$_3$ nanocomplex in cell culture medium over time (**A**) and in different pH solutions incubated for 24 h (**B**).
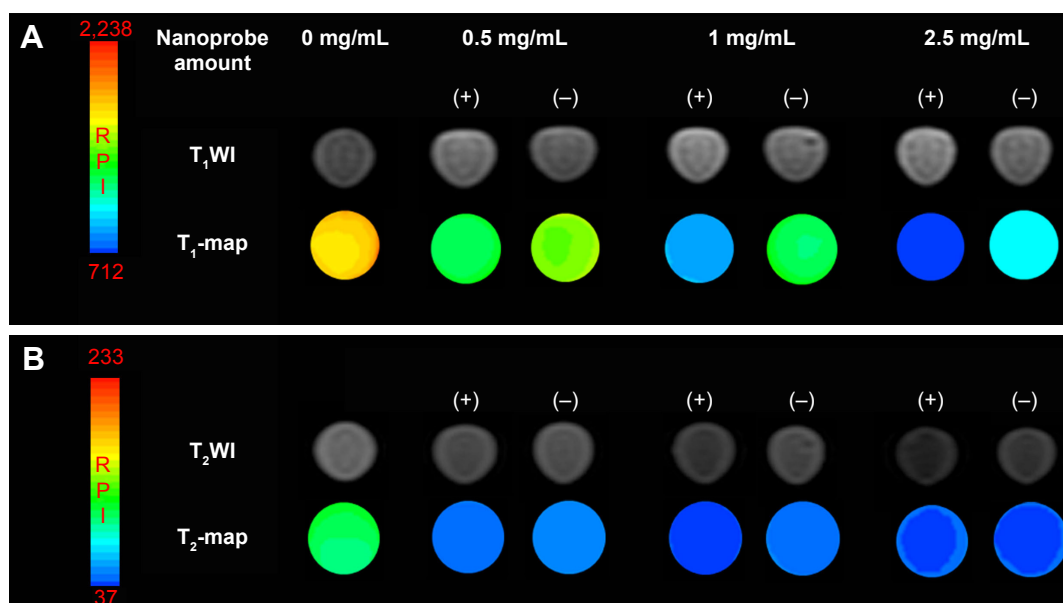
Figure 8 T_1-weighted magnetic resonance (MR) images and T_1-map images (**A**) as well as T_2-weighted MR images and T_2-map images (**B**) of 786-0 renal carcinoma cells treated with different concentrations of the Fe$_3$O$_4$@mSiO$_2$/PDDA/BSA-Gd$_2$O$_3$ nanocomplex (−) and Fe$_3$O$_4$@mSiO$_2$/PDDA/BSA-Gd$_2$O$_3$-AS1411 nanoprobe (+) (0, 0.5, 1, 2.5 mg/mL^{-1}). A 3.0 T human MR scanner was used.

The residual Gd concentrations in heart, liver, kidneys, and lungs were 1.90±0.12, 2.41±0.06, 2.15±0.08, and 2.27±0.1 µg/g at 1 h post-injection and 1.54±0.11, 1.94±0.12, 2.46±0.14, and 1.69±0.17 µg/g at 24 h post-injection, respectively.

In vivo toxicity evaluation

The in vivo toxicity of the Fe$_3$O$_4$@mSiO$_2$/PDDA/BSA-Gd$_2$O$_3$ nanocomplex was evaluated with standard hematologic and biochemical analyses and by referring to the literature.[45] Compared with the normal saline group, the HCT, HGB, RBC, WBC, MCV, MCH, and MCHC levels in the Fe$_3$O$_4$@mSiO$_2$/PDDA/BSA-Gd$_2$O$_3$ nanocomplex group showed no statistically significant differences, except for PLT (Figure 11). The ALT, AST, BUN, CREA, TP, ALB, and TBIL levels displayed no statistically significant difference between the normal saline group and the Fe$_3$O$_4$@mSiO$_2$/PDDA/BSA-Gd$_2$O$_3$ nanocomplex group (Figure 12).
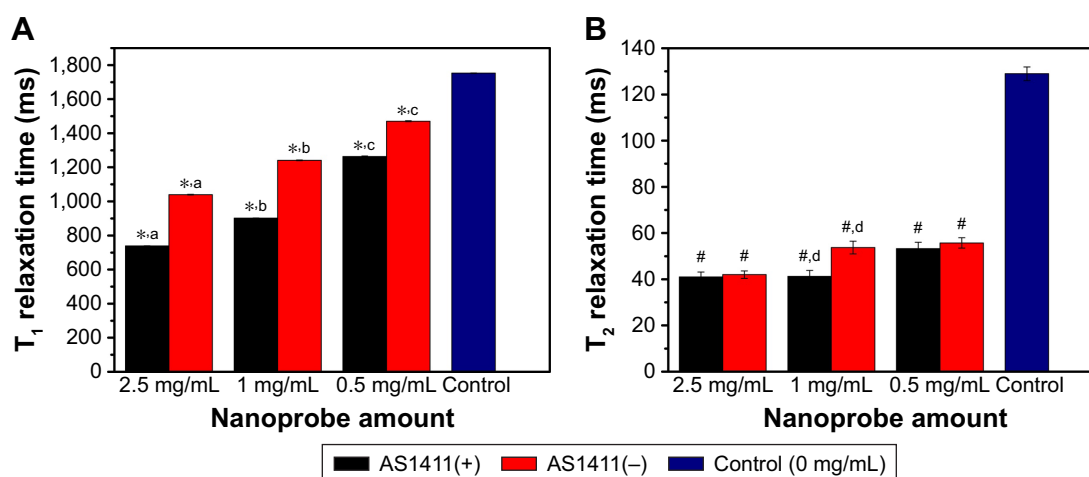

Figure 9 T_1 (**A**) and T_2 relaxation time (**B**) of 786-0 renal carcinoma cells treated with different concentrations of the Fe$_3$O$_4$@mSiO$_2$/PDDA/BSA-Gd$_2$O$_3$ nanocomplex (−) and Fe$_3$O$_4$@mSiO$_2$/PDDA/BSA-Gd$_2$O$_3$-AS1411 nanoprobe (+).
Notes: *Refers to statistically significant differences compared with the control group using one-way ANOVA ($p<0.05$). #Refers to statistically significant differences compared with the control group with one-way ANOVA ($p<0.05$). [a]Refers to statistically significant differences within group with LSD Duncan ($p<0.05$). [b]Refers to statistically significant differences within group with LSD Duncan ($p<0.05$). [c]Refers to statistically significant differences within group with LSD Duncan ($p<0.05$). [d]Refers to statistically significant differences within group with LSD Duncan ($p<0.05$). A 3.0 T human magnetic resonance scanner was used.
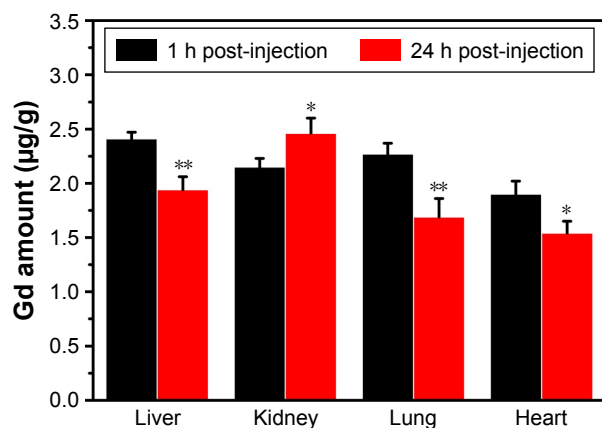
Figure 10 The concentrations of Gd in the heart, lung, liver, and kidney at 1 h and 24 h post-intravenous injection of the Fe_3O_4@$mSiO_2$/PDDA/BSA-Gd_2O_3 nanocomplex as determined by inductively coupled plasma-mass spectrometry (n=3, *$p<0.05$, **$p<0.01$).

In vivo MRI

For in vivo MR imaging, T_1 and T_2 dual-mode images were obtained pre- and post-injection of the Fe_3O_4@$mSiO_2$/PDDA/BSA-Gd_2O_3 nanocomplex using a 3T MR scanner at room temperature. MRI images were collected at scheduled intervals of 24 h post-injection. As shown in Figures 13 and S7, compared with the pre-injection reference, a darker signal in T_2-weighted images and a brighter signal in T_1-weighted images in the kidney at 15 min after administration were observed. However, at the 6-h time point, such signal contrasts in the kidney brought by the nanocomplex injection became weaker and the signal contrasts in the bladder became stronger, indicating that the excretion of the nanocomplex was mainly via the kidneys and bladder. These results showed the potential of the Fe_3O_4@$mSiO_2$/PDDA/BSA-Gd_2O_3

nanocomplex as an effective T_1–T_2 dual-mode CA for in vivo MRI with self-confirmation.

Discussion

T_1–T_2 dual modal MR imaging avoids the false-positive signals caused by a single imaging mode and provides more accurate and complementary information. The development of T_1–T_2 dual CAs favors T_1–T_2 dual modal MR imaging. However, interferences between the T_1 and T_2 CAs when they are in proximity would reduce their MRI relaxivity. To avoid this influence, a 20-nm $mSiO_2$ nanoshell was employed to increase the distance between T_1 CA, BSA-Gd_2O_3 NP and the T_2 CA, Fe_3O_4 NP in this study, because the interference of T_2 CA on the contrast enhancement of paramagnetic T_1 CAs might be weakened when their distance exceeds 12 nm. As expected, our fabricated Fe_3O_4@$mSiO_2$/PDDA/BSA-Gd_2O_3 nanocomplex presented a comparable T_1 relaxivity of 11.5 s^{-1} mM^{-1} to BSA-Gd_2O_3 (12.2 s^{-1} mM^{-1}), which was three times that of the commercial MRI CAs, Gd–DTPA (r_1=4.3 s^{-1} mM^{-1}). As reported, in a certain range, the larger the size of NPs, the stronger the saturation magnetization and relaxation rate of the nanomaterials.[46] In our work, the existence of PDDA favored more BSA-Gd_2O_3 NPs loading on the surface of Fe_3O_4@$mSiO_2$ NPs. Therefore, the T_1 relaxivity of the Fe_3O_4@$mSiO_2$/PDDA/BSA-Gd_2O_3 nanocomplex should be higher than that of pure BSA-Gd_2O_3 NPs. However, there was little difference of T_1 relaxivity between the Fe_3O_4@$mSiO_2$/PDDA/BSA-Gd_2O_3 nanocomplex and BSA-Gd_2O_3 NPs, which might arise from the interference of the Fe_3O_4 core, more or less. Besides the excellent MR imaging behaviors, the good biocompatibility and good stability in
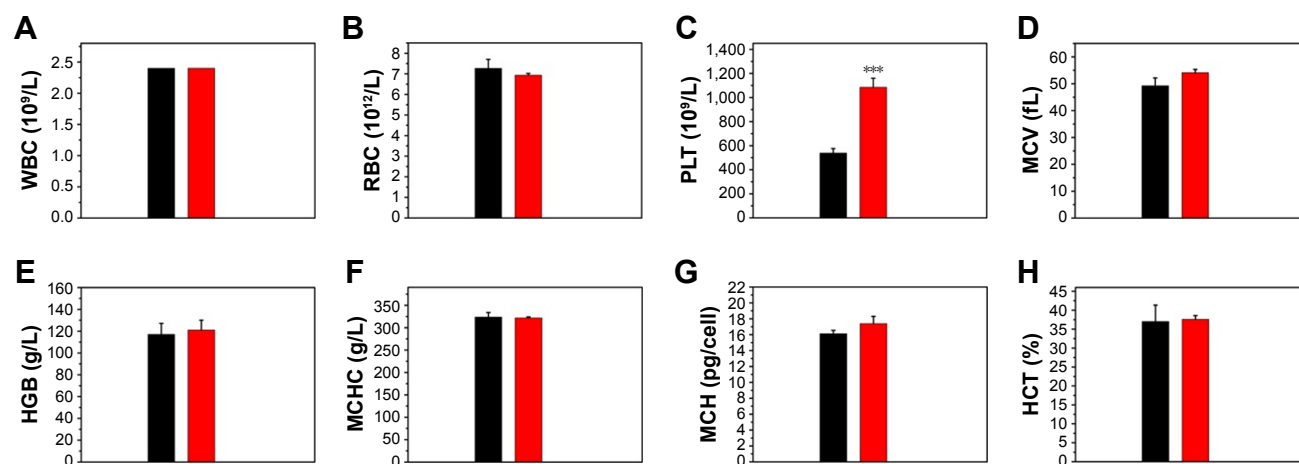

Figure 11 Hematologic analysis of mice at 1 week post-injection of normal saline (black bar) and the Fe_3O_4@$mSiO_2$/PDDA/BSA-Gd_2O_3 nanocomplex (red bar).
Notes: (**A**) White blood cells (WBC), (**B**) red blood cells (RBC), (**C**) platelets (PLT), (**D**) mean corpuscular volume (MCV), (**E**) hemoglobin (HGB), (**F**) mean corpuscular hemoglobin concentration (MCHC), (**G**) mean corpuscular hemoglobin (MCH), and (**H**) hematocrit (HCT) levels in the blood. ***Refers to statistically significant differences compared with the normal saline group ($p<0.001$, n=3).

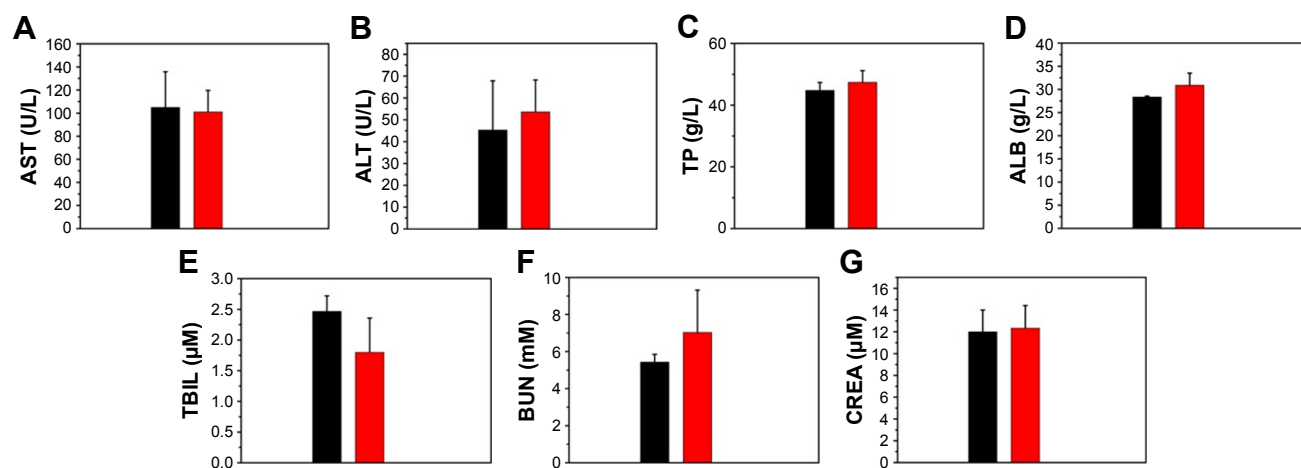**Figure 12** Biochemical analysis of mice at 1 week post-injection of normal saline (black bar) and the Fe_3O_4@mSiO$_2$/PDDA/BSA-Gd$_2$O$_3$ nanocomplex (red bar).
Notes: (**A**) Alanine transaminase (AST), (**B**) aspartate transaminase (ALT), (**C**) total protein (TP), (**D**) albumin (ALB), (**E**) total bilirubin (TBIL), (**F**) blood urea nitrogen (BUN), and (**G**) creatinine (CREA) levels in the blood; (n=3).

the cell culture medium or different pH solutions further provide the basis for their use to fabricate an mMRI nanoprobe. For hematologic analysis, all of the hematology markers displayed no statistically significant differences between the normal saline-treated group and the Fe_3O_4@mSiO$_2$/PDDA/BSA-Gd$_2$O$_3$ nanocomplex-treated group, except for PLTs. PLTs play a key role in hemostasis and thrombosis. Nanomaterials interact with PLTs and affect their count and
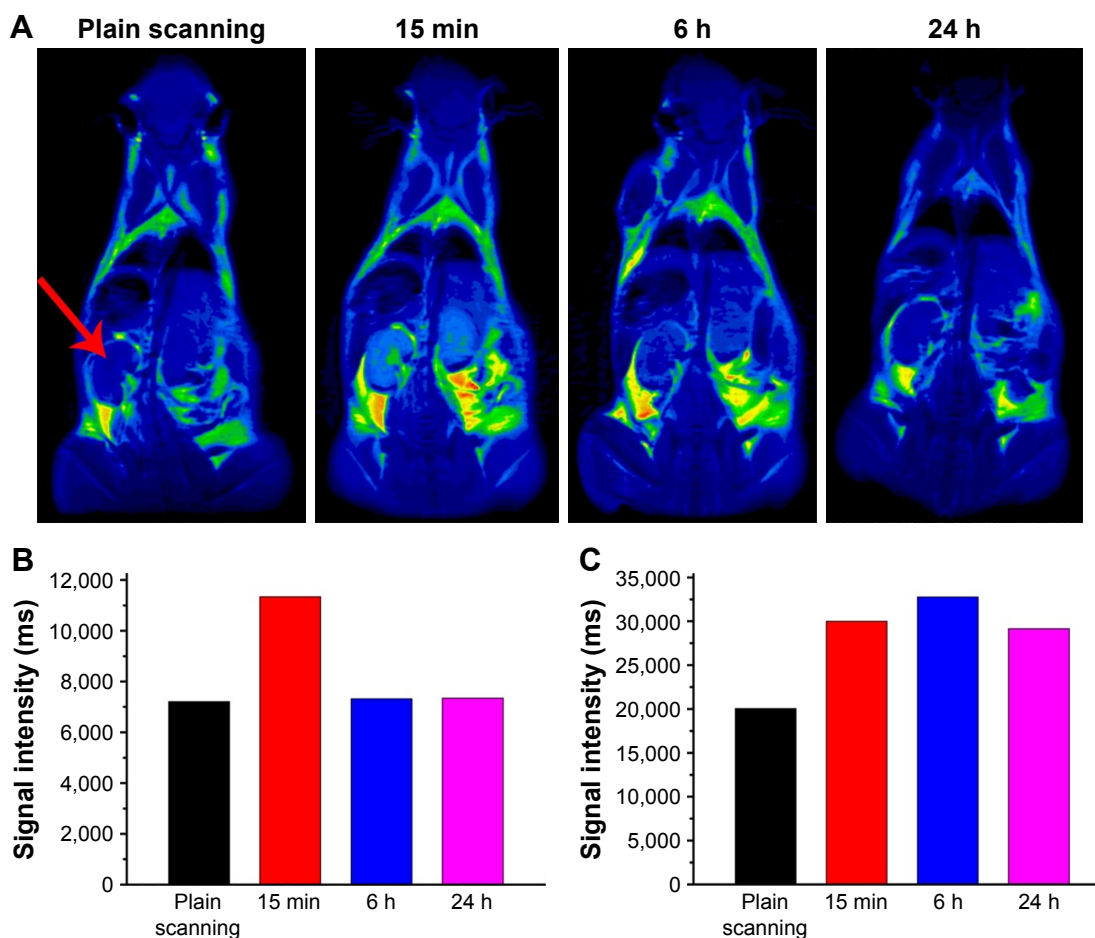

Figure 13 (**A**) T$_1$-weighted in vivo magnetic resonance imaging (MRI) images of mice post-injection of the Fe_3O_4@mSiO$_2$/PDDA/BSA-Gd$_2$O$_3$ nanocomplex at different time points (0, 15 min, 6 h, and 24 h). The signal intensities in the kidneys (**B**) and bladder (**C**) at different time points after intravenous injection of the Fe_3O_4@mSiO$_2$/PDDA/BSA-Gd$_2$O$_3$ nanocomplex. The red arrow indicates the kidney.

function, which might result in severe clinical outcomes.[47] For example, Radomski et al found multi- or single-walled carbon nanotubes (MWCNTs or SWCNTs) induced PLT activation and aggregation whereas C60 fullerences (nC60) had no effect.[48] Reinish et al observed a reduction in the PLT blood count in the first 5 min after the injection of negatively charged liposomes to rats, but noted a recovery of PLT count after 60 min post-injection.[49] Nanomaterial properties such as size, shape, chemical composition, and surface physicochemical property influence their effect on PLT, obviously. For biochemical analysis, the commonly used serum biochemical parameters including AST, ALT, TP, ALB, TBL, BUN, and CREA were measured. ALT and AST are commonly used indicators of liver function. Creatinine and BUN are important indicators of kidney function.[45] Compared with the normal saline-treated group, no statistically significant difference was observed in the above parameters in the $Fe_3O_4@mSiO_2/PDDA/BSA-Gd_2O_3$ nanocomplex-treated group, showing the good biocompatibility of $Fe_3O_4@mSiO_2/PDDA/BSA-Gd_2O_3$ nanocomplex in vivo. Then, after conjugation with the AS1411 aptamer as the targeting molecule, the 786-0 cells could be specifically targeted with the $Fe_3O_4@mSiO_2/PDDA/BSA-Gd_2O_3$-AS1411 nanoprobe by MRI. Furthermore, the $Fe_3O_4@mSiO_2/PDDA/BSA-Gd_2O_3$ nanocomplex could produce a signal enhancement in the kidney, suggesting their potential use as CAs in vivo. The biodistribution and clearance of nanomaterials in vivo is related to the characteristics of nanomaterials and organ specificity, such as hydrodynamic size, the surface charge, surface modification, and so on.[50–52] It was reported that NPs with a hydrodynamic diameter less than 5.5 nm could be excreted by renal clearance, and those with a hydrodynamic diameter more than 15 nm were usually captured and eliminated through the liver into bile and into feces.[53,54] However, in our case, the increase of Gd concentration in the kidney with time indicated the possible excretion route of the $Fe_3O_4@mSiO_2/PDDA/BSA-Gd_2O_3$ nanocomplex from the body through the kidneys, as even its hydrodynamic size was approximately 345.6 nm. This result was similar with that reported in Mekuria et al's report; they prepared $G4.5$-Gd_2O_3-PEG NPs with a hydrodynamic diameter of approximately 50 nm. They concluded that the kidneys removed NPs from the vascular compartment to the gall bladder.[55] This means the clearance route of nanomaterials was not only related to the hydrodynamic size, but also to other factors. The Gd concentrations in the heart, liver, and lung all decreased with time, as indicated by the gradual clearance of the $Fe_3O_4@mSiO_2/PDDA/BSA-Gd_2O_3$ nanocomplex from the body.

Conclusion

The introduction of CAs has improved the sensitivity of MRI greatly, stimulating its wider application in disease diagnosis. However, single-mode CAs are not yet perfected. The combination of T_1 and T_2 CAs can integrate the high tissue resolution of T_1 mode contrast imaging and the high feasibility of softer tissue detection of T_2 mode contrast imaging. Herein, to get a T_1–T_2 dual MRI CA with better signal enhancement effect, a $Fe_3O_4@mSiO_2/PDDA/BSA-Gd_2O_3$ nanocomplex was synthesized for better relaxivity of nano-CAs. The obtained nanocomplex displayed high longitudinal (r_1=11.47 mM s^{-1} Gd) and transverse (r_2=195.1 mM s^{-1} Fe) relaxivities, enabling its use as a T_1–T_2 dual CA for MRI. To further apply their use as mMR imaging nanoprobes for the specific recognition of tumor cells, the AS1411 aptamer which can specifically combine with the nucleolin of the surface of the tumor cell was covalently coupled with the $Fe_3O_4@mSiO_2/PDDA/BSA-Gd_2O_3$ nanocomplex. When intravenously injected into the mice, the $Fe_3O_4@mSiO_2/PDDA/BSA-Gd_2O_3$ nanocomplex could produce a kidney contrast-enhancement and was excreted via the bladder, thereby showing promise as a T_1–T_2 dual-mode CA.

Disclosure

The authors report no conflicts of interest in this work.

References

1. Weissleder R, Moore A, Mahmood U, et al. In vivo magnetic resonance imaging of transgene expression. *Nat Med*. 2000;6(3):351–355.
2. Weissleder R, Mahmood U. Molecular imaging. *Radiology*. 2001; 219(2):316–333.
3. Bellin MF. MR contrast agents, the old and the new. *Eur J Radiol*. 2006; 60(3):314–323.
4. Barandov A, Bartelle BB, Gonzalez BA, White WL, Lippard SJ, Jasanoff A. Membrane-permeable Mn(III) complexes for molecular magnetic resonance imaging of intracellular targets. *J Am Chem Soc*. 2016;138(17):5483–5486.
5. Phukan B, Mukherjee C, Goswami U, et al. A new bis(aquated) high relaxivity Mn(II) complex as an alternative to Gd(III)-based MRI contrast agent. *Inorg Chem*. 2018;57(5):2631–2638.

6. Boehm I, Heverhagen JT. Delayed reaction following gadolinium-based contrast agent application. *Magn Reson Imaging*. 2018;50:10–11.

7. Lee SH, Kim BH, Na HB, Hyeon T. Paramagnetic inorganic nanoparticles as T1 MRI contrast agents. *Wires Nanomed Nanobi*. 2014;6: 196–209.

8. Courant T, Roullin VG, Cadiou C, et al. Hydrogels incorporating GdDOTA: towards highly efficient dual T1/T2 MRI contrast agents. *Angew Chem Int Ed Engl*. 2012;51(36):9119–9122.

9. Na HB, Song IC, Hyeon T. Inorganic nanoparticles for MRI contrast agents. *Adv Mater*. 2009;21:2133–2148.

10. Cabana L, Bourgognon M, Wang JT, et al. The shortening of MWNT-SPION hybrids by steam treatment improves their magnetic resonance imaging properties in vitro and in vivo. *Small*. 2016;12(21): 2893–2905.

11. Laurent S, Forge D, Port M, et al. Magnetic iron oxide nanoparticles: synthesis, stabilization, vectorization, physicochemical characterizations, and biological applications. *Chem Rev*. 2008;108(6):2064–2110.

12. Terreno E, Castelli DD, Viale A, Aime S. Challenges for molecular magnetic resonance imaging. *Chem Rev*. 2010;110(5):3019–3042.

13. Liu Y, Chen Z, Liu C, Yu D, Lu Z, Zhang N. Gadolinium-loaded polymeric nanoparticles modified with Anti-VEGF as multifunctional MRI contrast agents for the diagnosis of liver cancer. *Biomaterials*. 2011;32(22):5167–5176.

14. Tasciotti E, Liu X, Bhavane R, et al. Mesoporous silicon particles as a multistage delivery system for imaging and therapeutic applications. *Nat Nanotechnol*. 2008;3(3):151–157.

15. Jun YW, Lee JH, Cheon J. Chemical design of nanoparticle probes for high-performance magnetic resonance imaging. *Angew Chem Int Ed Engl*. 2008;47(28):5122–5135.

16. Chen Y, Ai K, Liu J, Ren X, Jiang C, Lu L. Polydopamine-based coordination nanocomplex for T1/T2 dual mode magnetic resonance imaging-guided chemo-photothermal synergistic therapy. *Biomaterials*. 2016;77:198–206.

17. Keasberry NA, Bañobre-López M, Wood C, Stasiuk GJ, Gallo J, Long NJ. Tuning the relaxation rates of dual-mode T(1)/T(2) nanoparticle contrast agents: a study into the ideal system. *Nanoscale*. 2015; 7(38):16119–16128.

18. Huang G, Li H, Chen J, et al. Tunable T1 and T2 contrast abilities of manganese-engineered iron oxide nanoparticles through size control. *Nanoscale*. 2014;6(17):10404–10412.

19. Choi D, Han A, Park JP, et al. Fabrication of MnxFe1-xO colloidal solid solution as a dual magnetic-resonance-contrast agent. *Small*. 2009; 5(5):571–573.

20. Han A, Choi D, Kim T, et al. Fabrication of Mn-ferrite nanoparticles from MnO colloids. *Chem Commun (Camb)*. 2009;44:6780–6782.

21. Bae KH, Kim YB, Lee Y, Hwang J, Park H, Park TG. Bioinspired synthesis and characterization of gadolinium-labeled magnetite nanoparticles for dual contrast t1- and t2-weighted magnetic resonance imaging. *Bioconjug Chem*. 2010;21(3):505–512.

22. Choi JS, Lee JH, Shin TH, Song HT, Kim EY, Cheon J. Self-confirming "AND" logic nanoparticles for fault-free MRI. *J Am Chem Soc*. 2010; 132(32):11015–11017.

23. Yang H, Zhuang Y, Sun Y, et al. Targeted dual-contrast T1- and T2-weighted magnetic resonance imaging of tumors using multifunctional gadolinium-labeled superparamagnetic iron oxide nanoparticles. *Biomaterials*. 2011;32(20):4584–4593.

24. Zhou Z, Huang D, Bao J, et al. A synergistically enhanced T(1)–T(2) dual-modal contrast agent. *Adv Mater*. 2012;24(46):6223–6228.

25. Pierre VC, Botta M, Aime S, Raymond KN. Fe(III)-templated Gd(III) self-assemblies-a new route toward macromolecular MRI contrast agents. *J Am Chem Soc*. 2006;128(29):9272–9273.

26. Livramento JB, Tóth E, Sour A, Borel A, Merbach AE, Ruloff R. High relaxivity confined to a small molecular space: a metallostar-based, potential MRI contrast agent. *Angew Chem Int Ed Engl*. 2005;44(10): 1480–1484.

27. Livramento JB, Sour A, Borel A, Merbach AE, Tóth É. A starburst-shaped heterometallic compound incorporating six densely packed Gd³⁺ ions. *Chem Eur J*. 2006;12:989–1003.

28. Yang CT, Chuang KH. Gd(III) chelates for MRI contrast agents: from high relaxivity to "smart", from blood pool to blood-brain barrier permeable. *MedChemComm*. 2012;3(5):552–565.

29. Caravan P. Strategies for increasing the sensitivity of gadolinium based MRI contrast agents. *Chem Soc Rev*. 2006;35(6):512–523.

30. Davies GL, Kramberger I, Davis JJ. Environmentally responsive MRI contrast agents. *Chem Commun (Camb)*. 2013;49(84):9704–9721.

31. Ni K, Zhao Z, Zhang Z, et al. Geometrically confined ultrasmall gadolinium oxide nanoparticles boost the T(1) contrast ability. *Nanoscale*. 2016;8(6):3768–3774.

32. Ahmad MW, Xu W, Kim SJ, et al. Potential dual imaging nanoparticle: Gd2O3 nanoparticle. *Sci Rep*. 2015;5:8549.

33. Girvan AC, Teng Y, Casson LK, et al. AGRO100 inhibits activation of nuclear factor-kappaB (NF-kappaB) by forming a complex with NF-kappaB essential modulator (NEMO) and nucleolin. *Mol Cancer Ther*. 2006;5(7):1790–1799.

34. Ireson CR, Kelland LR. Discovery and development of anticancer aptamers. *Mol Cancer Ther*. 2006;5(12):2957–2962.

35. Bates PJ, Laber DA, Miller DM, Thomas SD, Trent JO. Discovery and development of the G-rich oligonucleotide AS1411 as a novel treatment for cancer. *Exp Mol Pathol*. 2009;86(3):151–164.

36. Kim DK, Mikhaylova M, Zhang Y, Muhammed M. Protective Coating of Superparamagnetic Iron Oxide Nanoparticles. *Chem Mater*. 2003; 15(8):1617–1627.

37. Kim J, Kim HS, Lee N, et al. Multifunctional uniform nanoparticles composed of a magnetite nanocrystal core and a mesoporous silica shell for magnetic resonance and fluorescence imaging and for drug delivery. *Angew Chem Int Ed Engl*. 2008;47(44):8438–8441.

38. Sun SK, Dong LX, Cao Y, Sun HR, Yan XP. Fabrication of multifunctional Gd2O3/Au hybrid nanoprobe via a one-step approach for near-infrared fluorescence and magnetic resonance multimodal imaging in vivo. *Anal Chem*. 2013;85(17):8436–8441.

39. Zhang PH, Cao JT, Min QH, Zhu JJ. Multi-shell structured fluorescent-magnetic nanoprobe for target cell imaging and on-chip sorting. *ACS Appl Mater Interfaces*. 2013;5(15):7417–7424.

40. Li J, You J, Dai Y, Shi M, Han C, Xu K. Gadolinium oxide nanoparticles and aptamer-functionalized silver nanoclusters-based multimodal molecular imaging nanoprobe for optical/magnetic resonance cancer cell imaging. *Anal Chem*. 2014;86(22):11306–11311.

41. Hao J, Song G, Liu T, et al. In vivo long-term biodistribution, excretion, and toxicology of PEGylated transition-metal dichalcogenides MS2 (M=Mo, W, Ti) nanosheets. *Adv Sci (Weinh)*. 2016;4(1):1600160.

42. Gao M, Li W, Dong J, et al. Synthesis and characterization of superparamagnetic Fe₃O₄@SiO₂ core-shell composite nanoparticles. *World J Condens Matter Phys*. 2011;1(2):49–54.

43. Li J, Jiang H, Yu Z, et al. Multifunctional uniform core-shell Fe3O4@mSiO2 mesoporous nanoparticles for bimodal imaging and photothermal therapy. *Chem Asian J*. 2013;8(2):385–391.

44. Wu C, Song J, Jiang C, Shen X, Qiao Q, Hu Y. Nucleolin targeting AS1411 modified protein nanoparticle for antitumor drugs delivery. *Mol Pharm*. 2013;10(10):3555–3563.

45. Zhang XD, Wu D, Shen X, et al. Size-dependent in vivo toxicity of PEG-coated gold nanoparticles. *Int J Nanomedicine*. 2011;6: 2071–2081.

46. Jun YW, Huh YM, Choi JS, et al. Nanoscale size effect of magnetic nanocrystals and their utilization for cancer diagnosis via magnetic resonance imaging. *J Am Chem Soc*. 2005;127(16):5732–5733.

47. Simak J, De Paoli S. The effects of nanomaterials on blood coagulation in hemostasis and thrombosis. *Wiley Interdiscip Rev Nanomed Nanobiotechnol*. 2017;9(5):e1448.

48. Radomski A, Jurasz P, Alonso-Escolano D, et al. Nanoparticle-induced platelet aggregation and vascular thrombosis. *Br J Pharmacol*. 2005;146(6):882–893.

49. Reinish LW, Bally MB, Loughrey HC, Cullis PR. Interactions of liposomes and platelets. *Thromb Haemost*. 1988;60(3):518–523.

50. van Schooneveld MM, Vucic E, Koole R, et al. Improved biocompatibility and pharmacokinetics of silica nanoparticles by means of a lipid coating: a multimodality investigation. *Nano Lett*. 2008;8(8):2517–2525.

51. Dai Y, Wu C, Wang S, et al. Comparative study on in vivo behavior of PEGylated gadolinium oxide nanoparticles and Magnevist as MRI contrast agent. *Nanomedicine*. 2018;14(2):547–555.

52. Shao Y, Tian X, Hu W, et al. The properties of Gd$_2$O$_3$-assembled silica nanocomposite targeted nanoprobes and their application in MRI. *Biomaterials*. 2012;33(27):6438–6446.

53. Fischer HC, Liu L, Pang KS, Chan WCW. Pharmacokinetics of nano-scale quantum dots: in vivo distribution, sequestration, and clearance in the rat. *Adv Funct Mater*. 2006;16(10):1299–1305.

54. Choi HS, Liu W, Misra P, et al. Renal clearance of quantum dots. *Nat Biotechnol*. 2007;25(10):1165–1170.

55. Mekuria SL, Debele TA, Tsai HC. Encapsulation of gadolinium oxide nanoparticle (Gd$_2$O$_3$) contrasting agents in PAMAM dendrimer templates for enhanced magnetic resonance imaging in vivo. *ACS Appl Mater Interfaces*. 2017;9(8):6782–6795.
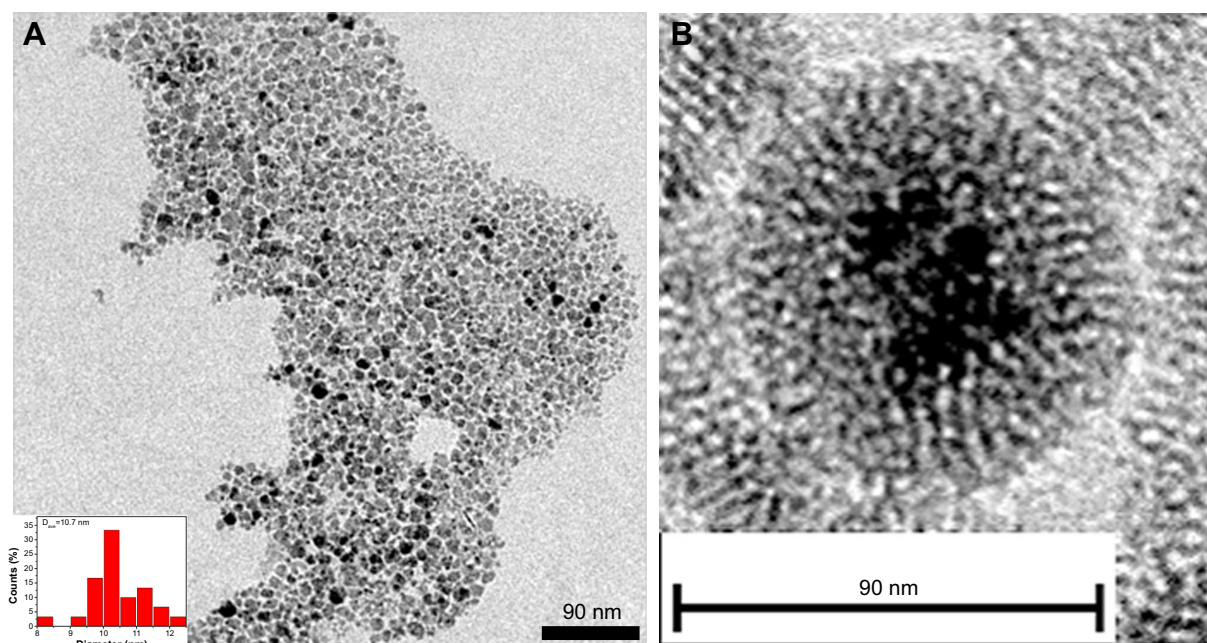
Supplementary materials

Figure S1 Transmission electron microscopy characterizations of Fe_3O_4 nanoparticles (NPs) (**A**) and $Fe_3O_4@mSiO_2$ NPs (**B**). The insert in (**A**) is the distribution of Fe_3O_4 NP size.
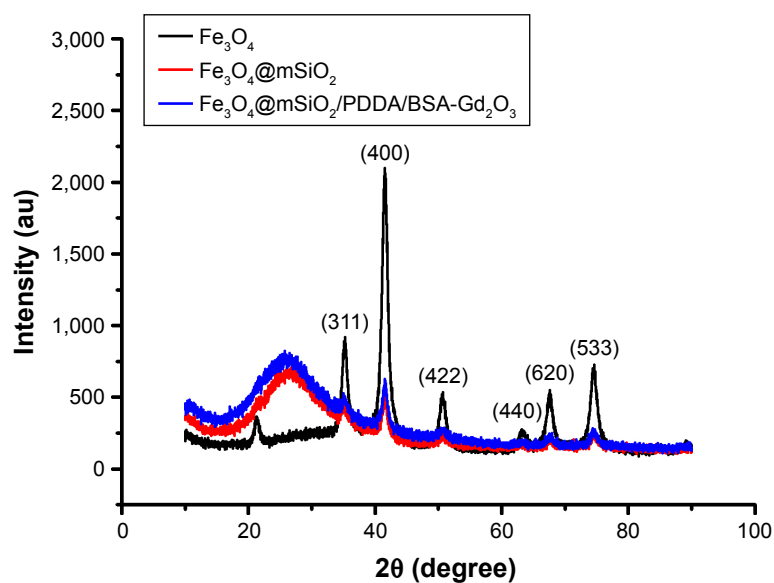
Figure S2 X-ray powder diffraction patterns of the Fe_3O_4, $Fe_3O_4@mSiO_2$ and $Fe_3O_4@mSiO_2/PDDA/BSA-Gd_2O_3$ nanocomplex.
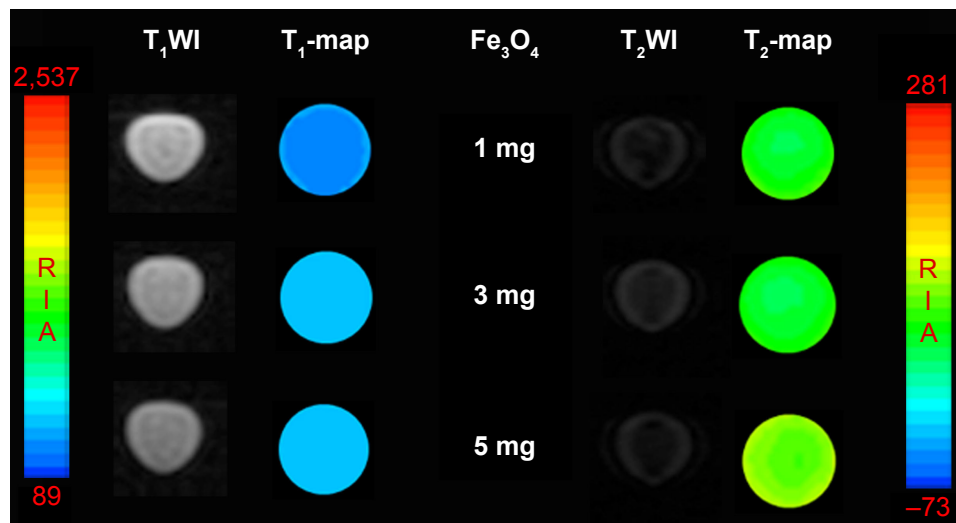
Figure S3 T_1-weighted magnetic resonance (MR) images and T_1-map images as well as T_2-weighted MR images and T_2-map images of the Fe_3O_4@$mSiO_2$/PDDA/BSA-Gd_2O_3 nanocomplex prepared with different concentrations of Fe_3O_4 nanoparticles. A 3.0 T human MR scanner was used.

Table S1 T_1 and T_2 relaxation time of the Fe_3O_4@$mSiO_2$/PDDA/BSA-Gd_2O_3 nanocomplex prepared with different concentrations of Fe_3O_4 nanoparticles ($\bar{X}\pm S$) (n=4)

Group	Fe_3O_4 concentration (mg)	T_1 relaxation time (ms)	T_2 relaxation time (ms)
1	1 mg	318.25±3.86	66.25±2.22
2	3 mg	448.75±7.93	65.25±2.50
3	5 mg	453.25±6.29	65.00±2.58
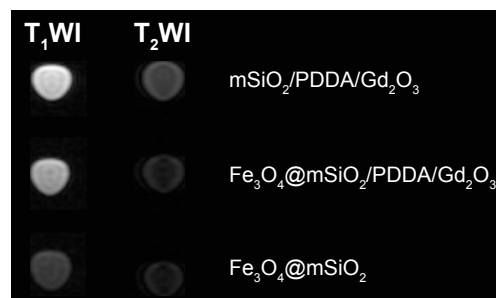
Figure S4 T_1-weighted magnetic resonance (MR) images as well as T_2-weighted MR images of the $mSiO_2$/PDDA/BSA-Gd_2O_3 nanocomplex, Fe_3O_4@$mSiO_2$/PDDA/BSA-Gd_2O_3 nanocomplex, and Fe_3O_4@$mSiO_2$ nanocomplex. A 3.0 T human MR scanner was used.

Table S2 T_1 and T_2 relaxation time of the $mSiO_2$/PDDA/BSA-Gd_2O_3 nanocomplex, Fe_3O_4@$mSiO_2$/PDDA/BSA-Gd_2O_3 nanocomplex and Fe_3O_4@$mSiO_2$ nanocomplex ($\bar{X}\pm S$) (n=4)

Group	T_1 relaxation time (ms)	T_2 relaxation time (ms)
$mSiO_2$/PDDA/Gd_2O_3	1,293.20±63.13*	557.00±15.58[a]
Fe_3O_4@$mSiO_2$/PDDA/Gd_2O_3	846.75±26.50[#]	146.50±26.25
Fe_3O_4@$mSiO_2$	219.50±5.80	149.25±12.63

Notes: *Refers to statistically significant differences when compared with the other two groups using one-way ANOVA ($p<0.05$). [#]Refers to statistically significant differences when compared with the other two groups using one-way ANOVA ($p<0.05$). [a]Refers to statistically significant differences when compared with the other two groups using one-way ANOVA ($p<0.05$).

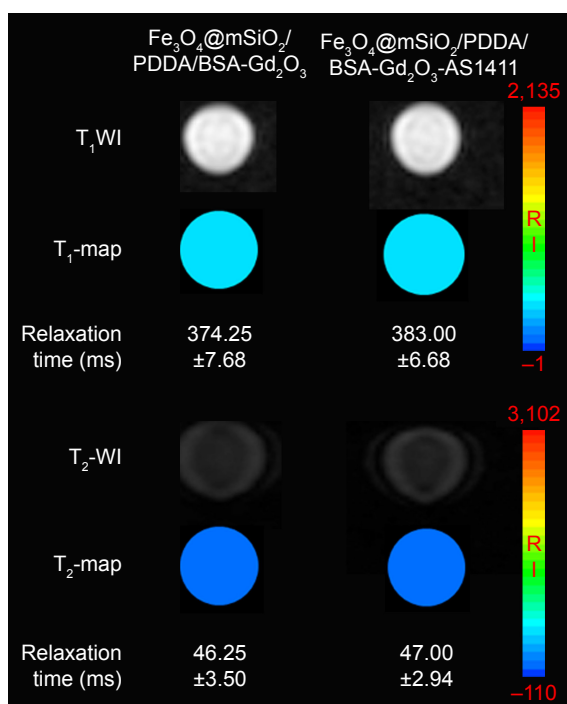**Figure S5** T$_1$-weighted magnetic resonance (MR) images and T$_1$-map images as well as T$_2$-weighted MR images and a T$_2$-map images of the Fe$_3$O$_4$@mSiO$_2$/PDDA/BSA-Gd$_2$O$_3$ nanocomplex and Fe$_3$O$_4$@mSiO$_2$/PDDA/BSA-Gd$_2$O$_3$-AS1411 nanoprobe. No significant difference of T$_1$ and T$_2$ relaxation time could be observed after the AS1411 aptamer modification. A 3.0 T human MR scanner was used.
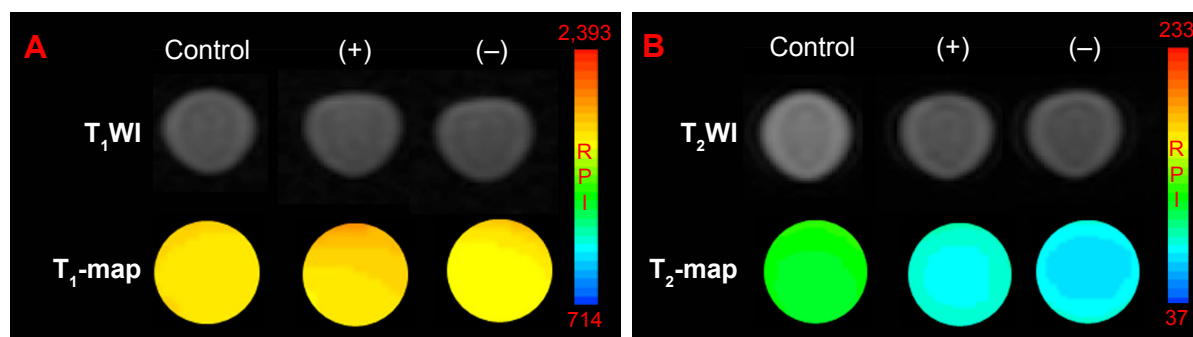

Figure S6 T$_1$-weighted magnetic resonance (MR) images and T$_1$-map images (**A**) as well as T$_2$-weighted MR images and T$_2$-map images (**B**) of NIH-3T3 cells treated with 1 mg mL^{-1} Fe$_3$O$_4$@mSiO$_2$/PDDA/BSA-Gd$_2$O$_3$ nanocomplex (−) and Fe$_3$O$_4$@mSiO$_2$/PDDA/BSA-Gd$_2$O$_3$-AS1411 nanoprobe (+). A 3.0 T human MR scanner was used.

Table S3 T$_1$ relaxation time of NIH-3T3 mouse fibroblast cells and 786-0 renal carcinoma cells treated with 1 mg mL^{-1} Fe$_3$O$_4$@mSiO$_2$/PDDA/BSA-Gd$_2$O$_3$ nanocomplex (−) and Fe$_3$O$_4$@mSiO$_2$/PDDA/BSA-Gd$_2$O$_3$-AS1411 nanoprobe (+) ($\bar{X}\pm S$) (n=4)

Group	NIH-3T3 cells	786-0 cells
Control	1,823.80±18.84	1,752.80±2.50
AS1411(+)	1,740.80±21.70*	902.25±2.21[#,a]
AS1411(−)	1,751.00±9.13*	1,241.20±3.40[#,a]

Notes: *Refers to statistically significant differences when compared with control group using one-way ANOVA ($p<0.05$). [#]Refers to statistically significant differences when compared with the control group using one-way ANOVA ($p<0.05$). [a]Refers to statistically significant differences between NIH-3T3 and 786-0 cells with LSD Duncan ($p<0.05$).

Table S4 T_2 relaxation time of NIH-3T3 mouse fibroblast cells and 786-0 renal carcinoma cells treated with 1 mg mL^{-1} Fe_3O_4@$mSiO_2$/PDDA/BSA-Gd_2O_3 nanocomplex (−) and Fe_3O_4@$mSiO_2$/PDDA/BSA-Gd_2O_3-AS1411 nanoprobe (+) ($\overline{X}\pm S$) (n=4)

Group	NIH-3T3 cells	786-0 cells
Control	132.50±9.95	129.00±2.94
AS1411(+)	67.00±2.16*	41.25±2.63[#,a]
AS1411(−)	65.50±2.65*	53.75±2.75[#,a]

Notes: *Refers to statistically significant differences when compared with the control group using one-way ANOVA ($p<0.05$). [#]Refers to statistically significant differences when compared with the control group using one-way ANOVA ($p<0.05$). [a]Refers to statistically significant differences NIH-3T3 and 786-0 cells with LSD Duncan ($p<0.05$).
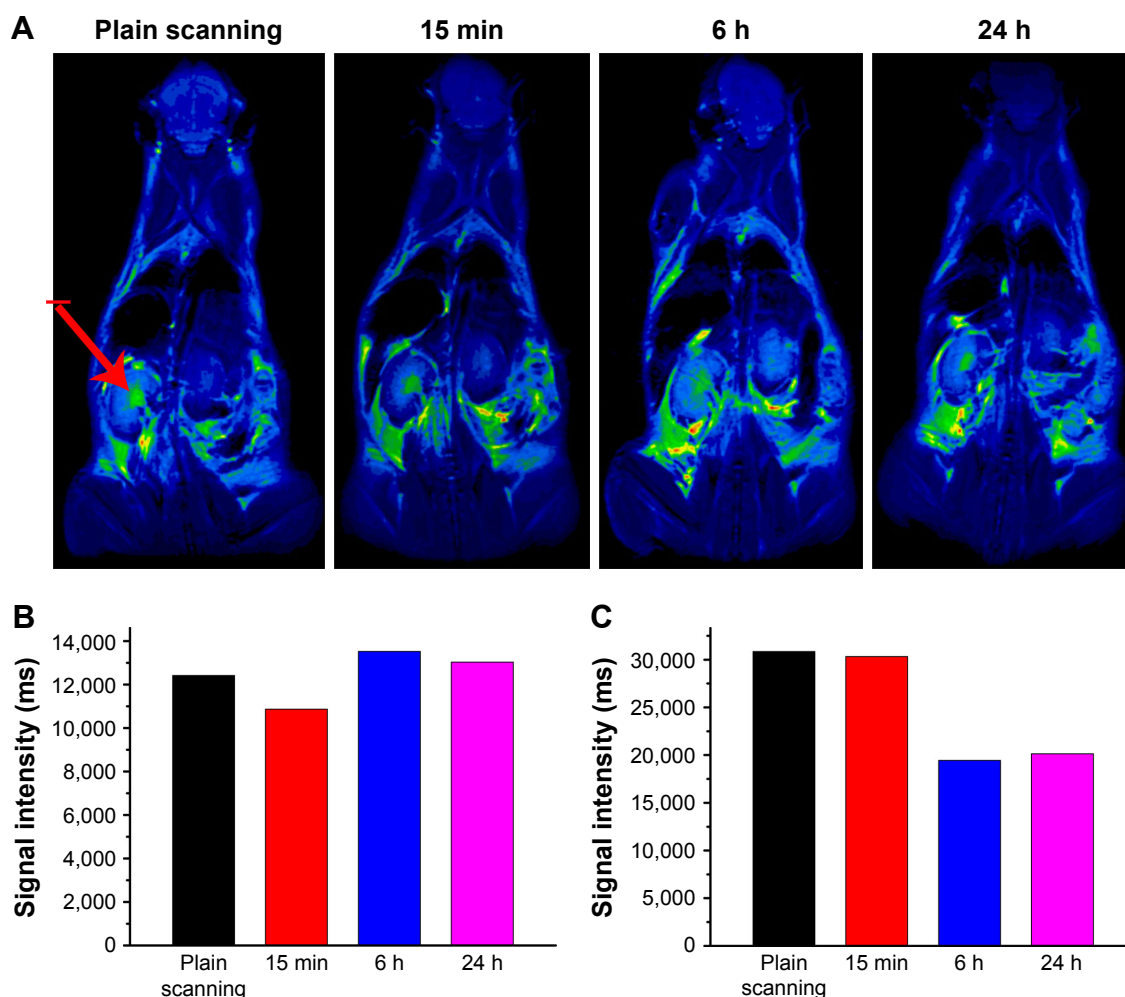

Figure S7 (**A**) T_2-weighted in vivo magnetic resonance imaging (MRI) images of mice post-injection of the Fe_3O_4@$mSiO_2$/PDDA/BSA-Gd_2O_3 nanocomplex at different time points (0, 15 min, 6 h, and 24 h). The signal intensities in the kidneys (**B**) and bladder (**C**) at different time points after intravenous injection of the Fe_3O_4@$mSiO_2$/PDDA/BSA-Gd_2O_3 nanocomplex. The red arrow indicates the kidney.